

Scalar mixing in a confined rectangular jet in crossflow

By M. W. PLESNIAK AND D. M. CUSANO

Purdue University, School of Mechanical Engineering, 585 Purdue Mall,
West Lafayette, IN 47907-2088, USA
plesniak@ecn.purdue.edu

(Received 21 July 2000 and in revised form 18 May 2004)

An experimental investigation of a confined rectangular jet in crossflow was performed. The rectangular jet is highly confined in that it spans almost 80% of the crossflow duct, rather than issuing into a semi-infinite crossflow. Furthermore, the jet is confined in the cross-stream direction because it issues into a relatively narrow duct. In addition, the flow rate of the secondary jet is large (up to 50% of the crossflow flow rate) which also influences the jet–crossflow interaction. Configurations of this type are found in a variety of different industrial manufacturing processes used to mix product streams.

A systematic variation of three pertinent parameters, i.e. momentum ratio, injection angle and development length, was performed. A full factorial experiment was run using three velocity ratios ($Vr = 0.5, 1.0, 1.5$), three downstream distances ($x/D_h = 6, 10, 19$) and six injection angles ($\alpha = 18^\circ, 24^\circ, 30^\circ, 48^\circ, 60^\circ, 90^\circ$). A planar Mie scattering mixing diagnostic system was used to evaluate the relative mixing effectiveness at various conditions within the parameter space studied. Three regimes for the jet–crossflow interaction and the resulting scalar concentration field were revealed: ‘wall jet’, ‘fully lifted jet’ and ‘reattached jet’. To understand the flow physics in these regimes, a more detailed exploration of the secondary flow and coherent structures was required. This was accomplished by acquiring velocity field data at measurement locations and conditions that demarcate the different regimes ($\alpha = 30^\circ$ and 48° , $Vr = 1.0$ and 1.5 , $x/D_h = 3, 6, 10, 15$ and 19) using a laser-Doppler velocimetry (LDV) system. The combined scalar concentration and velocity field data provided an understanding of the large-scale mixing and the role of coherent structures and their evolution. The investigation revealed that the flow does not necessarily develop symmetrically and also highlighted some of the effects of confinement.

1. Introduction and objectives

Jets discharging into crossflows are common in many engineering applications. Some examples include: smoke issuing from smokestacks; chimneys and volcanoes; waste water discharging into moving bodies of water; V/STOL aircraft in transition flight; dilution zones in gas turbine combustors; film cooling of turbine blades; gaseous state fuel injection; reaction control jets in rockets and missiles; and numerous manufacturing processes. These unique problems are geometric variants of the ‘classical configuration’: a round jet issuing perpendicularly into a semi-infinite uniform crossflow. The geometric variations can include differences in the jet shape, injection angle and the number of jets, as well as variations in the crossflow such as turbulence

level, swirl and confinement. Many important features of these flow fields, such as jet trajectory, spreading rates and momentum ratio effects have been investigated and characterized. In the wide variety of geometries studied, there is similarity in flow structures that develop.

This investigation of a confined rectangular jet-in-crossflow geometry is unique for several reasons. First, the rectangular jet spans almost 80% of the crossflow duct, rather than issuing into a semi-infinite crossflow (spanwise confinement). Secondly, the jet is confined in the cross-stream direction because it issues into a relatively narrow duct (cross-stream confinement). Thirdly, the flow rate of the secondary jet is large (mass flux ratio, $Mr = 0.17-0.53$) which also influences the jet-crossflow interaction. This complicated geometry is encountered in a variety of different industrial manufacturing processes used to mix two product streams. These processes are not designed to accomplish mixing on a molecular level, as in combustion applications, but rather to achieve macroscopic mixing, often, involving particles with a broad size distribution. Large-scale (integral length scale) flow structures, rather than small-scale structures, dominate the mixing of these particles. Therefore, experimental techniques capable of resolving molecular mixing, e.g. Raleigh scattering or planar laser induced fluorescence (PLIF), are not necessary to characterize mixing for these industrial applications. Small-particle-based techniques, such as those based on Mie scattering, are more appropriate for examining mixing processes at the macroscopic level.

A full-field planar optical diagnostic technique is used to study the mixing of a confined rectangular jet in crossflow. This Mie-scattering-based technique, developed by Eaton *et al.* (1996) for gas turbine premixers, was adapted for use in the present study. The rectangular jet is seeded with small tracer particles ($0.5\ \mu\text{m}$ aluminium oxide particles) and allowed to mix with the crossflow. A thin short-duration pulsed laser sheet illuminates a plane in the flow field and a digital camera captures the light scattered from the tracer particles. After processing the images, quantitative two-dimensional instantaneous scalar concentration field maps are obtained from the measured intensity distributions.

1.1. Literature review

Several review papers have been published on jets in crossflow (JICF) including those by Margason (1993), Holdeman (1993) and Sherif & Pletcher (1990). These papers reveal that while a variety of different geometries have been studied during the past fifty years, there have been relatively few regarding rectangular jets in crossflow, and even fewer regarding aspects of confinement. This paucity of literature on the case of interest requires a review of all related jet-in-crossflow configurations in order to gain an understanding of the expected flow behaviour of the current configuration. A brief review of pertinent literature is presented below.

1.1.1. Canonical round jet in crossflow

The earliest studies of jets in crossflow involved characterizing basic flow-field properties important for engineering applications, such as jet penetration and trajectory. In the past thirty years, the number of technological applications has greatly increased, inspiring a wide variety of studies. These studies examined the effects of momentum ratio, injection angle, skew angle, jet geometry, multiple jets, impingement and swirl.

The most obvious characteristic of the canonical round JICF is that the jet bends and aligns itself with the crossflow. Many authors (e.g. Jacquin 1994; Coelho & Hunt 1989; Morton & Ibbettson 1996) have noted that a jet cannot bend in the absence

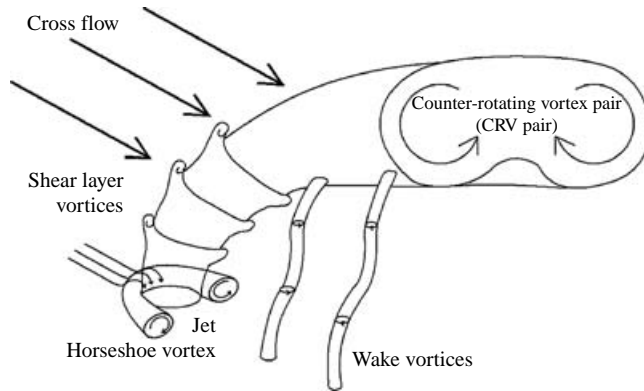


FIGURE 1. Vortical structures found in jets in crossflow.

of viscous effects, i.e. entrainment, separations, etc. As in free jets, entrainment is a critical phenomenon associated with the development of the JICF.

Crossflow jets are often used in situations to promote mixing and thus there is great interest in determining what influences scalar transport. In a comprehensive review, Holdeman (1993) considered the mixing of jets in crossflow and summarized the most important parameters. The impact of these parameters is as follows: (i) mixing was improved with downstream distance; (ii) the jet-to-crossflow momentum-flux ratio was the most significant flow variable; (iii) the effect of jet-to-crossflow density ratio appeared to be small at constant momentum-flux ratio; and (iv) smaller momentum-flux ratios required a greater downstream distance for equivalent mixing.

Fric & Roshko (1994) and others have characterized the following four main vortical structures that comprise the flow (figure 1): (i) shear layer vortices; (ii) horseshoe vortices; (iii) wake vortices (spin-off vortices); and (iv) counter-rotating vortex pair, or CRVP (also called kidney vortices and bound vortices). Peterson & Plesniak (2002, 2004) have documented the development of these structures from within the inlet plenum, through the injection hole and out into the crossflow, using particle image velocimetry. Other structures have also been reported. For example, Kelso, Lim & Perry (1998) Haven & Kurosaka (1996, 1997) and Kuzo (1995) and Hale, Plesniak & Ramadhyani (2000) have reported finding additional pairs of counter-rotating vortices. The traditional CRVP was bifurcated, with the extra pair(s) being located between the jet and the wall.

We will focus on the ubiquitous primary flow structures, the counter-rotating vortex pair. These large-scale vortical structures dominate the flow field. They remain in a plane normal to the jet trajectory and thus, eventually align themselves with the crossflow. Pratte & Baines (1968) noted that the effects of the CRVP could persist downstream as far as 1000 jet diameters. There are several points of view regarding the formation mechanism of these structures. The most well-established point of view was elucidated by Chang (1942) and later expanded upon by Margason (1969). A potential flow calculation was used to show that a cylindrical-shaped fluid boundary is deformed into the classical kidney shape resulting in a counter-rotating flow field. The shortcomings in this analysis include the lack of entrainment into the jet wake and the incorrect prediction of the induced pressure field in the plane of the jet exit. Other authors have computed jet properties with good accuracy using this theory by adding entrainment effects (e.g. Coelho & Hunt 1989; Leboeuf *et al.* 1991). Broadwell & Breidenthal (1984) provide another explanation of the CRVP formation mechanism

by drawing an analogy to a lift-generating body. The impulse of the jet can be viewed as providing a transverse force, such as that generated by a wing, which results in the vortex pair.

There are several proposed mechanisms for how the vorticity originating in the jet pipe stretches, reorients, or interacts with the vorticity of the incoming boundary layer resulting in the formation of the CRVP, most notably Jacquin (1994), Kelso *et al.* (1996), Morton & Ibbetson (1996) and Haven & Kurosaka (1996, 1997). Models that require interaction with the crossflow boundary layer should be dismissed because the CRVP occurs in elevated jets (e.g. smokestacks) which do not interact with a boundary layer (Eiff, Kawall & Keffer 1995). This is good example of how alternative configurations can aid in the understanding of the basic flow field.

The CRVP dominates the transport of the scalar field and thus the role of these structures in mixing must be reviewed to identify any possible implications on the present study. The main parameter influencing potential flow qualities (circulation and CRVP strength) is velocity ratio (Broadwell & Breidenthal 1984; Savory, Toy & Ahmed 1996). Related to these flow qualities are entrainment and maximum jet velocity decay rates, which both increase as velocity ratio increases (Patankar, Basu & Alpay 1977). Peak velocity within the deflected jet is coincident with the centres of the CRVP (Savory *et al.* 1996). The CRVP contains fluid originating from the approaching boundary layer, the jet and the free stream.

Margason (1993), in a review paper spanning fifty years of jet-in-crossflow research (313 references), summarized the best results for various important parameters, such as penetration, trajectory and mixing. While increasing jet penetration increases the rate of mixing between the jet and the crossflow, jet trajectory alone does not determine mixing effectiveness. Thus, the specifics of the mixing process must be examined throughout the range of jet trajectories. The jet often exhibits several behavioural zones as the trajectory varies from minimum to maximum values (see Sherif & Pletcher 1989, 1991). They pointed out that velocity ratio $Vr = 2$ seemed to be a borderline case between high and low velocity ratio jet behaviour. Lim, Kelso & Perry (1992) also noticed that changing velocity ratio from 1 to 5.5 produced two distinctly different flow structures. At high velocity ratios ($Vr > 2$), the jet was bent over far enough away from the injection wall so that there was little wall influence on its development. At low velocity ratio, i.e. $Vr < 1$, the jet behaves as a 'wall jet', meaning the jet is bent over and onto the injection wall immediately by the crossflow. There is a lack of a 'wake' region downstream of the jet injection hole. For $1 \leq Vr \leq 2$, the jet seems to be in an intermediate regime. In this regime, the jet can reattach to the injection wall. These results are of critical importance for mixing studies because the three regimes described above dictate the effectiveness of mixing. It should be noted that while the basic flow features do not change for the wide variety of geometries studied, the values of the controlling parameters do change. For example, a behaviour occurring at $Vr = 2.0$ for a round jet may occur at a different velocity ratio for another geometry.

Much of the computational effort in round jets has been concerned with predicting the gross flow-field characteristics such as jet penetration, spreading and mixing of a passive scalar. Almost all of these computations predict the gross flow field well using relatively simple turbulence models such as $k - \epsilon$, shown by Patankar *et al.* (1977) and Jones & McGuirk (1980). While the gross flow field can be predicted using the simplest turbulence models, the details of the CRVP are much more difficult to calculate. Reynolds stress models, i.e. solving transport equations for the Reynolds stresses, reproduce peak vorticity and CRVP strength very well, and predict Reynolds stresses better than $k - \epsilon$ models (Demuren 1992). Crabb, Duarão & Whitelaw (1981)

and Andreopoulos (1982) found regions of high streamline curvature, where the flow is locally anisotropic. In other locations, such as the wake, zero values in the shear stresses did not coincide with zero gradients of either mean velocity or turbulent kinetic energy, also indicating an anisotropic flow condition. These findings suggest that eddy viscosity and $k - \varepsilon$ models will be inadequate. Indeed, many computations succeed in capturing the CRVP, but not any other structures. Yuan (1997), Yuan & Street (1998) and Yuan, Street & Ferziger (1999), were among the first to use LES to compute this flow field. Among their results is a proposed mechanism for the formation of the far-field CRVP by means of the breakdown of quasi-steady vortices that extend upwards and downstream from the lateral edges of the jet.

Inclined JICF are studied mainly for V/STOL aircraft and film-cooling applications. The body of literature is extensive (see review by Cusano 1999). The noteworthy experimental work closely related to the issues in the current study includes: Krausche, Fearn & Westo 1978; Savory & Toy 1991; Holdeman 1993; Toy, Savory & McCusker 1993; Lee, Lee & Ro 1994. Simoneau & Simon (1993) reviewed the computational studies for film-cooling jet-in-crossflow applications. Some relevant computational studies involving multiple jets include those of Leylek & Zerkle (1994), Ajersch *et al.* (1995), and Sgarzi & Leboeuf (1997).

1.1.2. Rectangular jets in crossflow

Similarities between rectangular and round jets were evaluated to gain proper perspective of the round jet results to the present (rectangular) study. As it turns out, rectangular jets of aspect ratio = 1 behave nearly identically to round jets in terms of mixing effectiveness (Liscinsky, True & Holdeman 1996). Liscinsky *et al.* verified their results using two different concentration measurement techniques to show that Mie scattering results were similar to concentration measurements made using a point-wise probe.

Findlay *et al.* (1996) conducted an experiment similar to the present study. Their study focused on the behaviour of a row of inclined 30° square jets at velocity ratios of 0.5, 1.0 and 1.5. They found that outward spreading of the jet was not affected as greatly by velocity ratio as for vertical jets. Turbulent kinetic energy (TKE) distributions also did not change significantly with increasing velocity ratio. For the $Vr = 1.0$ case, TKE contours gave a better indication of spreading and penetration than did velocity contours. Surprisingly, they found no regions of circulation behind the jet (wake structure), which they attributed to asymmetric flow found in the jet hole.

Humber, Grandmaison & Pollard (1993) used marker nephelometry to study a sharp-edged rectangular jet with an aspect ratio of 10, at velocity ratios of 2.0 and 3.4. They outlined the following basic features of a rectangular jet in crossflow:

(i) The jet trajectory exhibits the initial high penetration region similar to a round jet, followed by a region further downstream where the trajectory is proportional to

$$\left(\frac{y}{Vr S}\right)^{0.17} \quad (1.1)$$

where S is the streamwise rectangular dimension.

(ii) Half concentration lengths (i.e. where $\bar{\Gamma}/\bar{\Gamma}_{max} = 0.5$) in the y and z planes follow linear and power law forms, respectively, as a function of the distance along the jet trajectory.

(iii) High levels of entrainment are indicated by mean decay of scalar concentration.

(iv) Concentration fluctuations are much higher in the cross-plane ((y, z) -plane) than in the streamwise plane ((x, z) -plane).

Nishiyama *et al.* (1993) performed a study on a 40 : 1 aspect ratio slot jet for velocity ratios of 0.2, 1.5 and 3.0. For $Vr=0.2$, the jet bends over and immediately attaches to the injection wall at a distance of $x/L=6$. There is no improvement in mixing with increased downstream distance. The $Vr=1.5$ case shows evidence of reattachment to the injection wall at $x/L=35$. At $Vr=3.0$, the jet is completely detached from the wall. It is of particular interest that the scalar field does not mix evenly about the jet centreline. As the velocity ratio is increased from 1.5 to 3.0, additional mixing occurs on the injection wall side of the jet. This explains why the proximity of the jet to the wall is so important. The closer the jet is to the wall, the greater the suppression of the large-scale structures in the wake of the jet and, ultimately, the lower the potential for mixing, assuming peak scalar concentration is at the jet centreline.

Weston & Thames (1979) compared the pressure field around rectangular and circular jets. They found that the streamwise-oriented slot generates a pressure profile similar to that of a round jet. This further substantiates the similarities reported in jet penetration and trajectory between the two shapes. Crossflow penetration and vortex strengths of cross-stream-oriented jets are less than those of streamwise-oriented jets at the same injection angle and velocity ratio. Crabb *et al.* (1981) reported that the proximity of the (confining) wall opposite the jet injection wall is very important owing to its impact on the pressure field.

Haven & Kurosaka (1996) point out that higher-aspect-ratio jets have lower trajectories, owing partly to the decreased degree of interaction between the counter-rotating vortex pairs. The closer the vortices, the stronger the mutual induction will be, propelling the vortices further from the injection wall. Increasing the aspect ratio likewise increases the vortex spacing. Kavsoglu, Schetz & Jakubowski (1989) also observed this phenomenon for rectangular jets with an aspect ratio of 0.25.

Simon & Ciancone (1985) performed the study that is perhaps the most geometrically similar to the current one. A variety of differently shaped jets at an injection angle of 30° and velocity ratios of 0.53, 1.1, 1.6, 4.1 and 6.2 were studied. An oblong jet with an aspect ratio of 2.73 was tested, in addition to a round jet and a cusp-shaped jet (the aspect ratio in the current geometry is 2.38). However, unlike the current study, their study did not have the additional complication of confinement. It was found that the round jet always penetrated further, for example, by $x/D=10$ the round jet penetrated twice as far into the crossflow as the oblong jet for the $Vr=1.1$ case. This effect was attributed to the increased pressure forces exerted on the oblong jet by the crossflow, and an increase in entrainment. Their results also showed that the oblong jet and the round jet spread at approximately the same rate, but that the oblong jet remained closer to the wall. Just as for normal jets, the spreading of the inclined jet is likely to be related to the size and strength of the CRVP and the associated crossflow entrainment.

1.1.3. Asymmetries in jets in crossflow

Various imposed and natural asymmetries of JICF structure have been reported in the literature. For example, compound angle injection is a widely used configuration in turbine film cooling which is known to produce an asymmetric CRVP. These skewed jets are also used as vortex generator jets (VGJ). Johnston & Khan (1997) and Khan & Johnston (2000) have obtained LIF images and LDV data to document the formation and evolution of a single dominant vortex in a VGJ configuration. A comprehensive review of VGJ is given by Johnston (1999). Of more interest to the

current study is the natural asymmetry that has been reported for jets that start from nominally two-dimensional conditions.

Kuzo (1995) and Smith & Mungal (1998) reported that the basic flow field associated with a single unconfined round jet in crossflow may not be a symmetric flow field. It may instead have very complex asymmetric states depending on parameters such as Reynolds number and velocity ratio. The body of evidence for a natural asymmetric flow state is not large because very often experimentalists and computational researchers assume flow symmetry, and examine only a half-plane of the flow.

Both Kuzo (1995) and Smith & Mungal (1998) investigated jets over a range of velocity ratios of 5–25 and a range of Reynolds numbers (Re_D) of 2000–40 000. The geometric configurations were symmetric in all measurable and quantifiable respects. Kuzo (1995) reported the ‘existence of mean flow fields which do not constitute a vortex pair’. Using digital particle image velocimetry (DPIV) and laser induced fluorescence (LIF), entire velocity fields were measured and imaged at various cross-sections downstream of the jet. Some of the key features discovered, in addition to the canonical symmetric CRVP, were (i) unsteadiness, i.e. spatial variation in the location of the vortices in different realizations of the velocity field, (ii) asymmetry in the strength and location of the CRVP, even when it was spatially stationary, and (iii) the occurrence of ‘secondary and tertiary vortices’, which were one or more vortices in addition to the CRVP. A ‘critical’ Reynolds number divided the asymmetric regime from the symmetric one. Unsteadiness was associated with flow conditions that were close to this ‘critical’ Reynolds number. It is important to note that the geometric configuration was held constant in this study, while the jet velocity ratio and Reynolds number were varied, so that the same apparatus produced both symmetric and asymmetric mean flows depending on flow conditions. The authors speculated that the asymmetry might be associated with the tertiary structures or with asymmetry in the upstream horseshoe vortex.

Smith & Mungal (1998), (see also Smith *et al.* 1993; Smith 1996) focused on the mixing field associated with a round jet in crossflow over a range of parameters similar to that used by Kuzo. Planar laser induced fluorescence (PLIF), with acetone as the marker species, was used to measure molecular mixing of the jet with the crossflow over a range of Reynolds numbers of 16 600–33 000 and velocity ratios of 5–25. Asymmetric distributions (about the spanwise centreline) of the jet fluid concentration were found in ensemble-averaged end views. The CRVP was rarely symmetric in shape or concentration, with one of the vortices becoming dominant. The peak concentration of the dominant vortex was as much as twice that its partner in the CRVP. The asymmetry ‘remained the same in degree and direction’ over many days of data acquisition. Figure 2 shows variation in the spatial position of the CRVP at instants in time, along with the ensemble-averaged result in the top left-hand image. Smith & Mungal (1998) also report ensemble-averaged results for various parameters and clearly show asymmetry in the mean scalar concentration field, as well as in the instantaneous variations.

The authors checked the initial conditions and geometry for asymmetry, but none was found. It was also observed that jets from the same nozzle and crossflow conditions exhibited both symmetric and asymmetric profiles at different locations downstream. They concluded that although the experimental set-up is symmetric to laboratory accuracy, the structures associated with the jet are asymmetric. Unlike Kuzo (1995), these authors found no trend with Reynolds number that divided the symmetric from the asymmetric state. They also cited a substantial body of evidence

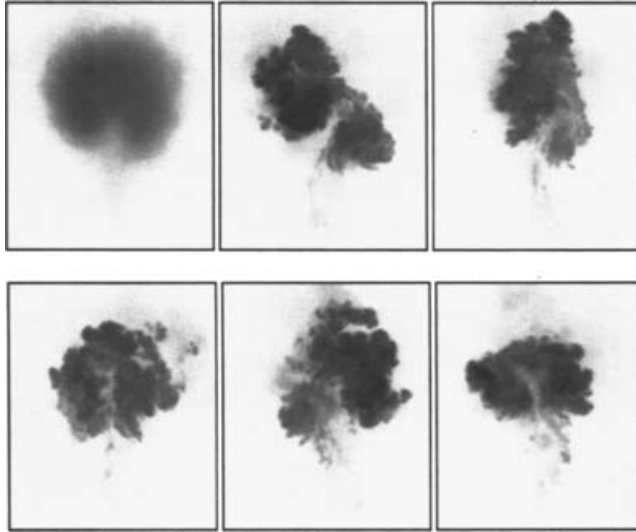


FIGURE 2. Ensemble-averaged (top left) and instantaneous end views for $Vr = 10$, (Smith *et al.* 1993).

in the literature indicating that the average concentration profiles in transverse jets were not symmetric about the spanwise centreline ($z = 0$), including those of Eiff *et al.* (1995), McCann & Bowersox (1996) and Liscinsky *et al.* (1996). Smith & Mungal concluded that ‘creating a transverse jet flow field that is symmetric about $z = 0$ is not regularly accomplished in laboratory studies, thus the determination of the ultimate symmetry or asymmetry of the transverse jet is an open question’.

Hence, a growing body of evidence indicates that the flow field created by a jet in crossflow is not inherently symmetric (even in the mean sense). It has been shown that the CRVP structures vary in size, location and strength (figure 2). These fluctuations have previously been assumed to be equivalent for both counter-rotating vortices. New studies indicate that symmetric geometries can produce flows that are symmetric (in the mean) for certain flow conditions and streamwise locations, but are asymmetric for other conditions and streamwise locations.

1.2. Summary and objectives

Despite extensive work over the past five decades, a complete understanding of the flow physics of even the classical JICF configuration is still lacking. For instance, the origin of the hallmark flow feature, the counter-rotating vortex pair, still remains a topic of debate. One reason for the lack of complete understanding is the highly turbulent separated three-dimensional nature of the flow field. This not only hampers experimental measurements, but also causes difficulty in simulating the flow numerically. These difficulties limit the insight that can be gained from additional studies of the canonical case and emphasize the importance of studying alternative, often more complex configurations that exhibit similar flow structures. Results from alternative configurations can then be applied to enhance understanding of flow physics and mixing in the canonical problem.

The primary goal of this experimental study was to investigate the flow physics and scalar mixing in a confined rectangular jet in crossflow, a complex configuration of considerable technological interest, which has not previously been reported in the literature. Although the geometry appears to be a hybrid between a confined JICF

and that of two intersecting ducts, the bypass of fluid around the gap at the top and bottom of the secondary duct/main duct intersection is critical in causing JICF-like behaviour, including formation of the CRVP. The following objectives were defined to achieve this goal:

(i) Perform a parametric study by varying the control parameters (velocity ratio, injection angle and streamwise development distance) to determine their effects on the scalar transport and mixing characteristics of the flow field.

(ii) Classify different regimes of JICF development and behaviour in terms of relevant control parameters.

(iii) Measure the velocity field associated with coherent structures in the JICF and evaluate their effects on mixing.

(iv) Evaluate the effects of confinement on the flow physics, scalar mixing, behavioural regimes and trajectory by comparing the present results to unconfined JICF results in the literature under comparable conditions.

2. Experimental apparatus and instrumentation

A versatile facility was constructed to perform experiments over a range of parameters of interest in typical manufacturing processes that use rectangular jets in crossflow for mixing products. The parameters varied were: velocity ratio, intersection angle and development length (these are defined in figure 6). Velocity ratio[†] is defined by $Vr = V_j / V_c$, where V_j is the average bulk velocity of the secondary duct (jet) and V_c is that of the main duct (crossflow). In addition to the baseline condition ($Vr = 1.0$), two other velocity ratios were investigated (0.5 and 1.5). The velocity of the secondary duct was changed to achieve these velocity ratios, while the main duct velocity remained constant for each case. Six intersection angles between the main and secondary duct were investigated: 18°, 24°, 30°, 48°, 60° and 90°. The effects of development length on the mixing process were evaluated by making scalar concentration field and velocity field measurements at several locations downstream of the jet-crossflow intersection.

2.1. Flow facility

The flow facility (figure 3) consists of two ducts and an intersection section supplied by a compressed air source. All test-section components are made from optically clear, scratch-resistant acrylic sheet (DuPont SAR) to facilitate optical diagnostic measurements. The main duct is 57.2 mm wide and 76.2 mm tall ($D_h = 65.3$ mm), while the secondary duct is 25.4 mm wide and 60.5 mm tall ($D_h = 35.7$ mm). Both the main and secondary ducts were designed to achieve fully developed mean velocity profiles ($x/D_h \approx 30$) before their intersection in order to achieve well-defined inflow boundary conditions. Measurements using laser Doppler velocimetry (LDV) confirmed that the mean velocity profiles were self-similar (Cusano 1999). Access slots with leak-tight covers were machined into the tops of all the main duct sections at 15.24 cm intervals for probe access. Both ducts are connected to the upstream supply plenums via contractions based on fifth-order polynomial shapes (Mehta & Bradshaw 1979) and the flow exits through a diffuser. Flow conditioning, consisting of high-pressure-drop Scotch-brite material followed by a flow-straightener made of plastic honeycomb was provided in both upstream plenums to reduce disturbances.

[†] Since the fluid temperature and pressure (and hence the density) of both streams is the same, momentum ratio is equivalent to velocity ratio squared.

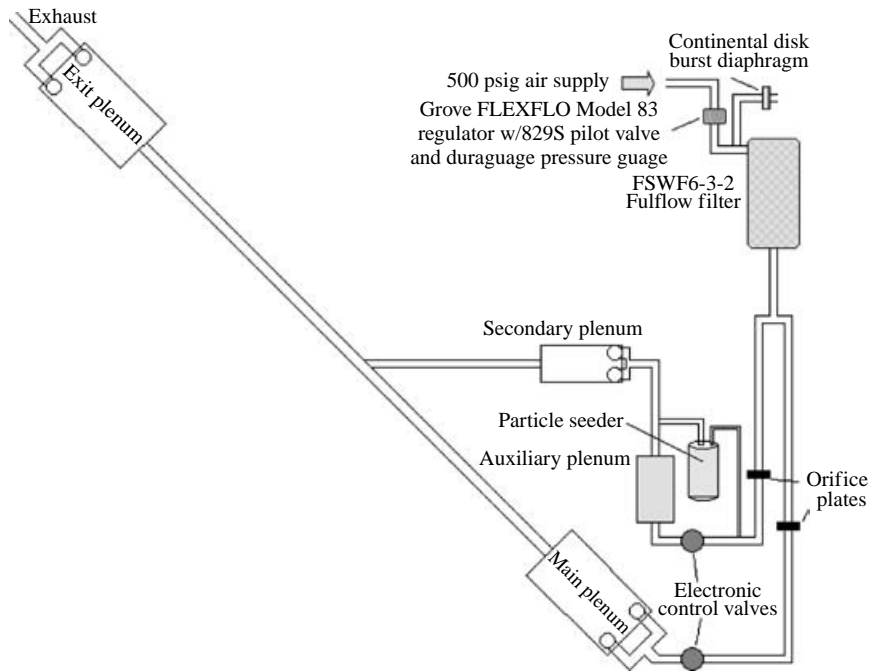


FIGURE 3. Flow schematic for experimental apparatus.

The air is supplied at a maximum pressure of 3.4 MPa (500 psig.) and flows through nominal 5.08 cm (2 in) diameter schedule 40 steel pipe. A Grove FLEXFLO Model 83 regulator maintains a pressure of 792.9 kPa (115 psia) during operation. Downstream of the valve, the flow is filtered with a model FSF6-3-2F Fulflow Filter, rated for a maximum pressure of 1.03 MPa (150 p.s.i.) to remove particles larger than $0.3\ \mu\text{m}$. After filtration, the supply line tees into individual feed lines for the main and secondary duct flows. At a distance of 45 diameters downstream of the closest elbow, the flow in each duct is metered by an ASME standard (Bean 1971) sharp-edged orifice flow meter. The air static temperature is also measured using an Omega type K thermocouple. The flow rate in the main duct is controlled by a Johnson Controls (VB 3754-5, CV 13.9) gate valve with a Johnson Controls Model VB-74002 electric actuator.

The secondary duct flow must be seeded with tracer particles to perform the Mie-scattering mixing diagnostics. Aluminium oxide particles (Al_2O_3), with a mean diameter of $0.5\ \mu\text{m}$, are used for seeding the flow. The particles were introduced into the secondary duct air supply by a reverse cyclone seeder initially designed according to Kounalakis (1990). The original design was modified in order to improve seeder performance and output. The modified seeder produces a constant flow with a particle concentration fluctuation less than 10%. The seeder modifications and performance tests are described in Eaton (1995). The air for the particle seeder is bled from the secondary duct supply line through a port located downstream of the orifice plate. After the seeder supply take off, the flow proceeds through a Johnson Controls Model (VB 3754-4, CV 8.6) gate valve with a Johnson Controls Model VB-74002 electric actuator and into the plenum supplying the secondary duct.

The air flow-control system was designed to deliver inlet air to the main and secondary duct inlet plenums at various operating conditions summarized in table 1.

Parameter (SI, English)	Main duct		Secondary duct
	Upstream of intersection	After intersection	
Height (S) (mm, in)	76.2, 3.0	76.2, 3.0	60.45, 2.38
Width (L) (mm, in)	57.15, 2.25	57.15, 2.25	25.4, 1.0
Aspect ratio (S/L)	1.33	1.33	2.38
Flow rate (kg s^{-1} , lb s^{-1})	0.243, 0.536	0.329, 0.725	0.086, 0.189
Flow area (cm^2 , in^2)	43.5, 6.75	43.5, 6.75	15.4, 2.38
Velocity (m s^{-1} , ft s^{-1})	45.7, 150	61.6, 202	45.7, 150
D_h (mm, in)	65.28, 2.57	65.28, 2.57	35.81, 1.41
Re (D_h)	2.04×10^5	2.76×10^5	1.12×10^5
Re (S)	2.38×10^5	3.22×10^5	1.89×10^5
Re (L)	1.78×10^5	2.41×10^5	7.94×10^4

TABLE 1. Experimental run conditions ($Vr = 1.0$).

The flow-control system is comprised of a National Instruments Lab PC + DAQ board and a personal computer running National Instruments Labview software. The two output channels of the DAQ board provide excitation for the two electric actuators on the supply line flow control valves, which sets the desired flow rate.

2.2. Experimental techniques

This study uses several experimental techniques: Mie-scattering-based scalar concentration measurements, laser-Doppler velocimetry (LDV), Pitot-static probe measurements, and flow visualization. Except for the Mie-scattering technique, the techniques are well developed and widely used.

2.2.1. Mie-scattering-based scalar concentration measurements

The applicability of the Mie-scattering technique to a flow field similar to the current study was demonstrated by Liscinsky & True (1994) and Liscinsky *et al.* (1996). Using gas concentration measurements and a Mie-scattering technique, they established that the two methods yielded identical results within the error bounds of their experiment. The Mie-scattering technique for scalar concentration measurement is based on the assumption that the scattered light received by the detector is linearly proportional to the number of particles in the measurement volume (see Becker 1977 for a review of marker nephelometry). The average number density must be small enough for independent scattering to occur, yet large enough so that the particle size distribution in the control volume is the same everywhere at the same instant (Shaughnessy & Morton 1977). With these criteria met, the degree of linearity is governed entirely by the concentration of particles.

The lower limit on particle concentration is related to the resolution of the Mie-scattering technique. Spatial resolution of the technique is limited by marker shot noise (Rosensweig, Hottel & Williams 1961) and is due to the fact that there is a finite number of markers within a volume and that this number varies with time. Marker shot noise is inversely proportional to the square root of the number of particles per unit volume (Long, Chu & Chang 1981). Fortunately, there is a wide range between the upper and lower limits to avoid secondary scattering and marker shot noise. According to Long *et al.* (1981), the minimum and maximum concentrations observed in their experiment were 1.67×10^5 and 1.4×10^{13} particles/ mm^3 , respectively, i.e. eight orders of magnitude within which to set the particle concentration levels.

The intensity of light scattered from the particles is directly related to the local instantaneous scalar concentration when the following conditions are met:

- (i) Laser pulse duration is short enough to ‘freeze’ the axial motion of the particles.
- (ii) Particles follow the flow scales of interest.
- (iii) Particle seeding requirements (concentration) are met.

Because ‘instantaneous’ concentration measurements are required, the laser sheet must be of short enough duration to ‘freeze’ the flow. Using the highest velocity in either duct, 91 m s^{-1} , and the ruby laser’s pulse duration (30 ns), it is estimated that the particles will move axially an average of $3 \mu\text{m}$ during the duration of the laser pulse. Comparing that length to the thickness of the laser sheet ($\approx 500 \mu\text{m}$), it is reasonable to assume that the measurements are instantaneous.

Samimy & Lele (1991) performed direct numerical simulations of the Navier–Stokes equations in conjunction with experiments made using a Mie-scattering technique. They showed that the Mie-scattering technique accurately resolves (large-scale) vortical structures in turbulent compressible shear layers for values of the particle Stokes number, τ_r , ranging from 0.05 to 0.25. Here, τ_r is defined as the ratio of the particle response time to the fluid response time. The authors gave a criterion for choosing appropriately sized particles to study this flow by requiring that $\tau_r \leq 0.5$.

For a conservative estimate, τ_r should be based on the worst-case particle size (largest) and flow scales (shortest duration). The response time for the particles (assuming Stokes drag) is given by:

$$\tau_p = \frac{\rho_p d_p^2}{18\mu}, \quad (2.1)$$

where ρ_p is the particle density, d_p is the (maximum) particle diameter, and μ is the fluid viscosity. The flow time scale is given by:

$$\tau_f = \frac{L_v}{U_v}, \quad (2.2)$$

where L_v is the eddy length scale and U_v is the eddy velocity scale (Crowe, Gore & Troutt 1985).

The ratio of these two time scales for the worst-case combination of test parameters in this study is 0.047, which falls within the stated guidelines for accurate tracking of the flow by the particles.

Planar mixing diagnostics system. The planar mixing diagnostics system is comprised of a laser light source, a flow seeded with appropriately sized tracer particles and a camera system to record the scattered light intensity distribution. In this experiment, only the secondary duct was seeded with particles, which effectively tag the secondary duct fluid. A second camera and a cell containing a laser fluorescent dye is used to measure and record the laser sheet energy distribution (see figure 4). The images are post-processed, resulting in a quantitative two-dimensional planar concentration measurement. Large-scale mixing of the secondary duct fluid with that of the main duct is inferred from the measured scalar concentration distribution.

The light source is a Q-switched Lumonics HLS-0.6 pulsed ruby laser operated to produce a 0.4 J pulsed beam (duration of 30 ns at a wavelength of 694 nm) that is expanded into a sheet and used to illuminate the plane of interrogation. The entire sheet-forming optical train is mounted on an optical breadboard designed to translate to the desired downstream location. A -45 mm focal length, plano-concave cylindrical lens expands the beam into a sheet approximately 15.25 cm high before it

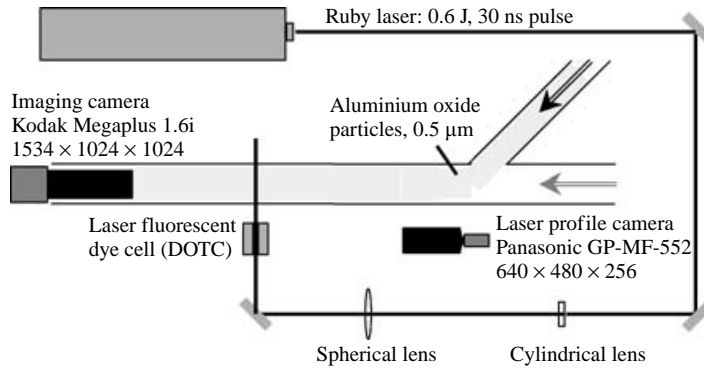


FIGURE 4. Mie scattering experimental set-up. (Note that the camera is not inserted into the test section.)

is collimated using a 600 mm focal length, plano-convex spherical lens. A spatial filter then clips the beam to a height of 7.62 cm. A large gold-coated mirror (fixed at 90°) directs the beam into the laser fluorescent dye cell, and then through the main duct. The beam converges along the propagation direction at an angle of less than 10° to a (measured) waist, which is ≤ 1 mm thick, located at the centre of the duct. The beam then diverges at the same angle through the rest of the interrogation region. A beam dump is placed on the other side of the duct to minimize optical noise.

The ruby laser produces a beam with a Gaussian intensity profile (i.e. spatially non-uniform intensity) with varying total energy output for each pulse. An image of the sheet energy distribution (from top to bottom) is required for image processing to account for variations in beam shape and power. A fluorescing dye contained in an optical-quality cell ($100 \times 50 \times 40$ mm BK-5 fused glass cell, Helma Cells Inc. Model 740.000) is located in the optical path. The fluorescing dye is an approximately 2×10^{-11} molar solution containing 0.1 mg of DOTC perchlorate per litre of propylene carbonate (both supplied by Exciton). Using a low concentration eliminates beam attenuation by the dye and ensures that dye fluorescence is linear with incident energy.

The mixing images are captured using a Kodak Megaplug 1.6i digital camera and a Matrox Pulsar PCI frame-grabber board with a slave ISA RS-422 digital interface card. Laser-fluorescent dye cell images are captured using a Panasonic GPMF-552 CCD camera and Matrox Meteor RGB PCI frame-grabber board. All boards were operated simultaneously in a Pentium 166 MHz personal computer. The Kodak Megaplug 1.6i camera has an pixel array of 1534 (H) by 1024 (V) pixels with a 100% fill ratio, and 1024 grey levels. Each pixel is $9 \times 9 \mu\text{m}$, yielding an image size of $13.8 \text{ mm} \times 9.2 \text{ mm}$. A 75–300 mm f/4.5 Tamaron zoom lens provides a full-frame mixing image at all measurement stations. Optical distortions are often severe with zoom lenses, but this drawback is alleviated because the pixel array covers only the central 25% of the image. Field curvature and spherical aberration are negligibly small in this region. The frame grabber was externally triggered using a TTL signal, derived from the oscillator output on the ruby laser. The mixing image camera shutter was used in inverse mode, that is, the shutter is normally open and the trigger signal causes it to close and the frame to be transferred to the frame-grabber board. This required the experiment to be run in a darkened room to minimize background noise.

Image processing software. After acquiring the images, post-processing is required to extract quantitative concentration information. Corrections are required for the

following:

- (i) Non-uniform object plane illumination: laser power fluctuations, sheet energy profile variations, laser sheet non-uniformity.
- (ii) Solid and scattering angle variations across the mixing image.
- (iii) Miscellaneous noise sources: secondary scattering from the walls, and electronic noise.

The procedure used to compensate for laser intensity variations has already been described. Mie-scattering theory results were implemented in a software package to calculate scattering and solid angle correction multipliers. The program uses the phase angle method to solve Maxwell's equations (simplified for the Mie-scattering regime) to give the intensity distribution of coherent polarized light, scattered from spherical particles at different angles with respect to the detector. The code accounts for the solid-angle differences that occur horizontally across the CCD camera array (typically 1–5%). Note that variations vertically across the CCD array owing to Mie scattering are $< 0.5\%$ and therefore can be neglected. The code outputs a vector of 1534 multipliers to correct each image for scattering and solid-angle intensity variations. All the aforementioned parameters are dependent only on geometry, therefore the code was run once for each streamwise measurement station and the same correction array is used for all images taken at that station.

To minimize electronic and background noise, a background image without the flow or particles was acquired. The only objects that are imaged are the walls of the duct, which scatter light when the laser sheet passes through them. Several of these images were averaged and the resulting composite background image subsequently subtracted from every mixing image. To minimize the effects of secondary scattering from particle deposition on the walls during the actual tests, the perimeter of the image was masked out during image processing. This area extends approximately 3 mm into the duct from the walls.

2.2.2. LDV methodology

A Dantec two-component fibre optic LDV system was used to acquire velocity data. This system consisted of: a three-axis computer-controlled motorized traverse, a fibre optic LDV probe with a 2X beam expander and 600 mm lens, a model FVA signal processor, a 500 mW argon ion laser and a beam splitter providing two sets of beams at 488 and 522 nm, and a 486DX-100 personal computer running Floware software.

The Floware software package interfaced with the traverse controller and the FVA unit to actuate the probe, then store the data received from the FVA unit. Data from the FVA unit are taken using settings in the Floware software package.

To facilitate comparisons with the scalar concentration data, the velocity field was interrogated in planes at the same locations as the mixing images. In order to document the streamwise development of the flow patterns, intermediate planes not included in the mixing data test matrix were also measured. This provided the complete flow-development history sampled at equal downstream intervals that also overlap with three mixing locations.

Because three-dimensional data were necessary to gain insight into the complex flow phenomena, the probe was oriented in two orthogonal planes allowing all three velocity components to be acquired, two at a time. The (U, V) -plane (defined in figure 5) data were taken with the beams propagating through the sidewall. The (U, W) -plane data were taken by reflecting the beams off a mirror oriented at 45° from the horizontal and mounted directly under the test section (see figure 5). Thus, the probe

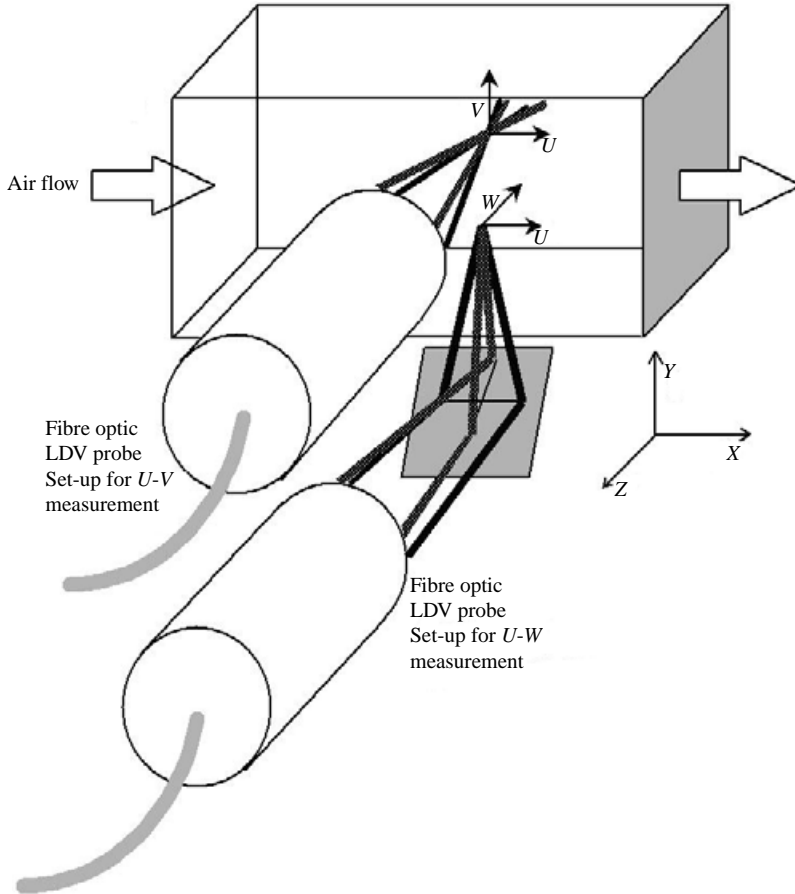


FIGURE 5. LDV fibre optic probe set-up.

was kept in the same vertical plane, facilitating alignment of the two measurement planes.

The measurement grid consists of 112 points with a sampling time of 30 s at each point. The test rig and particle seeder were run continuously at a fixed flow rate during the time necessary to acquire data at all points in the measurement grid. The three-dimensional flow data at each streamwise location is the result of two separate data acquisition events spanning a period of 3 to 4 hours. Both the main and secondary air streams were seeded with aluminium oxide particles to ensure adequate seeding levels. Sampling rates varied from 10 samples/s to 10 000 samples/s. Data rates dropped at near-wall grid points owing to noise generated by secondary reflections caused by the walls. Typically, a minimum of 1000 samples were collected at each probe position. All flow quantities of interest can be computed from the velocity data, except for the secondary Reynolds shear stress $\langle v'w' \rangle$, which would require simultaneous sampling of the V and W velocity components.

To improve the fidelity of the results, a 3-sigma software filter was applied to the time record of velocity to remove spurious realizations. Any individual realization more than 3 standard deviations (sigma) from the mean value was discarded. Once this was accomplished, mean velocity (U_{mean}), root mean square (r.m.s.) velocity (U_{rms}),

and higher-order statistical quantities are calculated using residence weighted time-averaging to reduce the velocity bias in the measurements.

2.3. Experimental uncertainty

Experimental uncertainty was estimated following the methods of Kline & McClintock (1953) and Moffat (1988). First-order uncertainty estimates were verified from repeatability experiments. Detailed uncertainty calculations are given in Cusano (1999).

There are two uncertainty-related issues in the air flow system: how accurately the flow can be measured and how accurately the flow rate can be set with the valve actuators. The accuracy of the flow measurements depends on the combined accuracy of the two pressure transducers and the thermocouple used to make measurements, and the accuracy of the empirical relation used to compute velocity from the measured pressure difference. The total uncertainty in the calculated flow rate is $\pm 1.3\%$. Flow rate could be adjusted by the actuators within $\pm 1.1\%$ of the set point. Hysteresis was observed to be as large as $\pm 3\%$. The precision of the controllers was excellent, as settings were easily repeated to within 0.25% .

Uncertainty for the Mie-scattering diagnostic system is comprised of two parts: the accuracy of the measurement and the accuracy of the post-processing procedure. The accuracy of the imaging camera is defined by the number of grey levels that the camera is capable of resolving and the image intensity. The mixing image camera can resolve 1024 grey levels and operates at an average grey level of 300 for a relative resolution of 0.3% . The laser-fluorescent dye cell camera can resolve 256 grey levels and operates at an average grey level of 110 for a relative resolution of about 1% . Assuming ideal processing, the total uncertainty for the data acquisition system is $\pm 1.3\%$. The total accuracy of post-processing is about $\pm 0.8\%$. The total uncertainty for the planar mixing diagnostic system is then $\pm 2.1\%$ (within an individual image). Accuracy among sets of images will be affected by the number of images in a particular data set, as well as contributors such as particle seeding anomalies. Overall accuracy of the system in measuring mean scalar concentration was $\pm 5\text{--}7\%$, based on repeatability tests.

A velocity field acquired in the secondary duct with the LDV taken at two different times was used to test the total accuracy of the system, including alignment. The streamwise mean velocity (U) was repeatable to within 1% (standard deviation) at every point in the measurement grid. The same accuracy was achieved with the U - W velocity probe orientation. At every plane there is a redundant U velocity measurement. The two probe orientations typically measure the U_{mean} velocity to within 1% (0.7% standard deviation). Overall accuracy of the measurements are between 1 and 5% .

3. Results

Scalar concentration field measurements were taken at three velocity ratios ($Vr = 0.5, 1.0, 1.5$), three downstream distances ($x/D_h = 6, 10, 19$) and six injection angles ($\alpha = 18^\circ, 24^\circ, 30^\circ, 48^\circ, 60^\circ, 90^\circ$) in a full factorial test matrix (54 experiments). A schematic illustrating these parameters is shown in figure 6. Complementary velocity field measurements were taken at conditions where the transition from one flow regime to another was identified by the scalar field data. Flow-visualization experiments were conducted as well, but are not reported herein (see Cusano 1999).

The scalar concentration data also revealed an unexpected result: pronounced asymmetry in the scalar field was found for some 30° and larger injection angle cases.

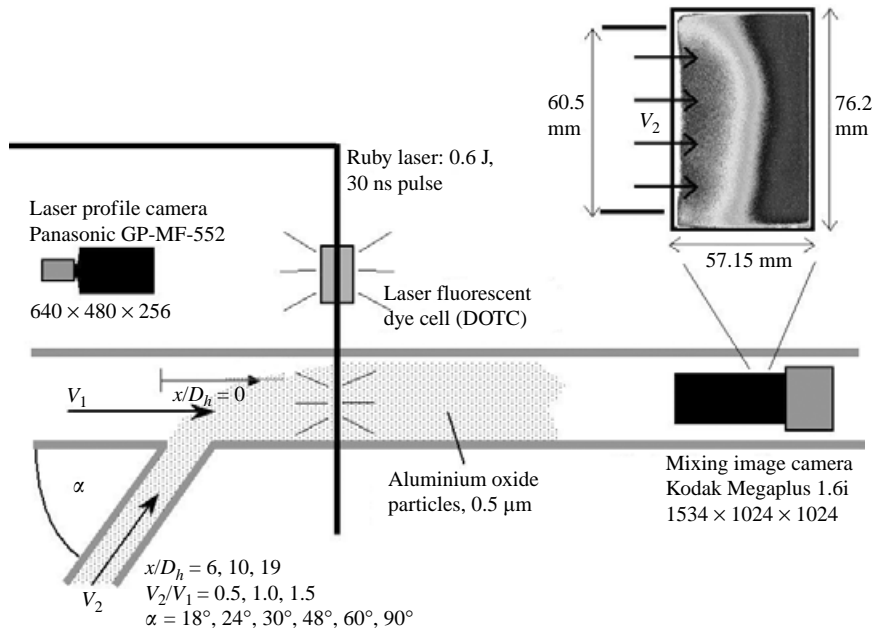


FIGURE 6. Mie scattering mixing measurement locations.

Velocity field data verified that the flow field was asymmetric, but they did not provide an explanation for the cause for the asymmetry. As indicated in § 1, asymmetric flow behaviour has been observed under a variety of different conditions. Asymmetric states can be natural occurrences or they can be induced by boundary conditions, such as skew angle. An effort was made to identify the nature of the asymmetry in the flow. After identification of several possible asymmetry drivers, various laboratory tests were carried out to quantify the effect of these factors on scalar concentration.

3.1. Scalar concentration field

In all of the plots presented, the secondary jet enters from the left-hand edge of the picture and the observer's point of view is looking upstream (towards the intersection) at the cross-sectional plane specified, so that the main flow is out of the page. To quantify mixing, sets of 15–20 individual images were acquired and averaged together to form a composite image. This ensemble size was verified to be sufficient to achieve stationary mean concentration values (Cusano 1999). The composite image was normalized by the average intensity, which represents a perfectly mixed value, assuming ideal mixing. This normalization enables results to be compared directly among the various cases within the error bounds of the experiment (± 5 –7%). Composite images consisting of up to 1024 grey levels are rescaled to improve contrast. An example showing individual realizations of instantaneous images is shown in figure 7. Note the differences in the intensity distributions for each realization.

While composite images provide a good measure of time-averaged mixing performance, the time-varying or unsteady nature of the flow field is lost. However, the counter-rotating vortices fluctuate considerably, which impacts the mixing process. This can be evaluated qualitatively by comparing each of the individual realizations in figure 7. To quantify this important feature of the flow field, concentration fluctuation maps were calculated following the procedure of Rathgeber & Becker (1983).

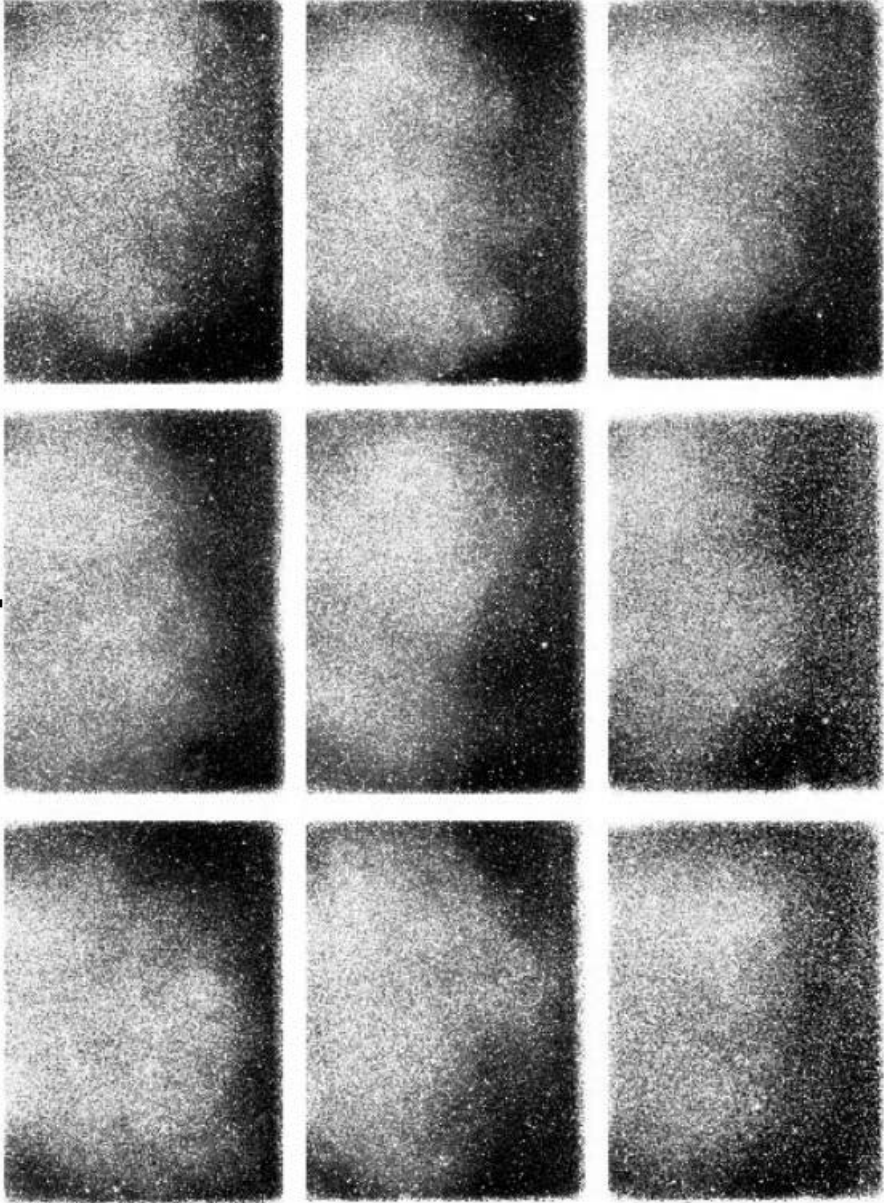


FIGURE 7. Individual realizations of raw scalar concentration (intensity) for $\alpha = 30^\circ$, $x/D_h = 10$, $Vr = 1.5$.

Concentration fluctuation is defined as:

$$C' = \frac{\hat{\gamma}}{C_{mean}} \quad (3.1)$$

where $\hat{\gamma}$ = r.m.s. value of C about C_{mean} and C_{mean} is the average concentration.

To calculate the r.m.s. concentration fluctuation, concentration images were re-sampled on a grid sufficient to resolve the integral length scale of the flow. Because C' is a statistical (r.m.s.) quantity, an adequate sample size is required to achieve convergence. The data sets consist of 15–20 images, with r.m.s. calculations conducted

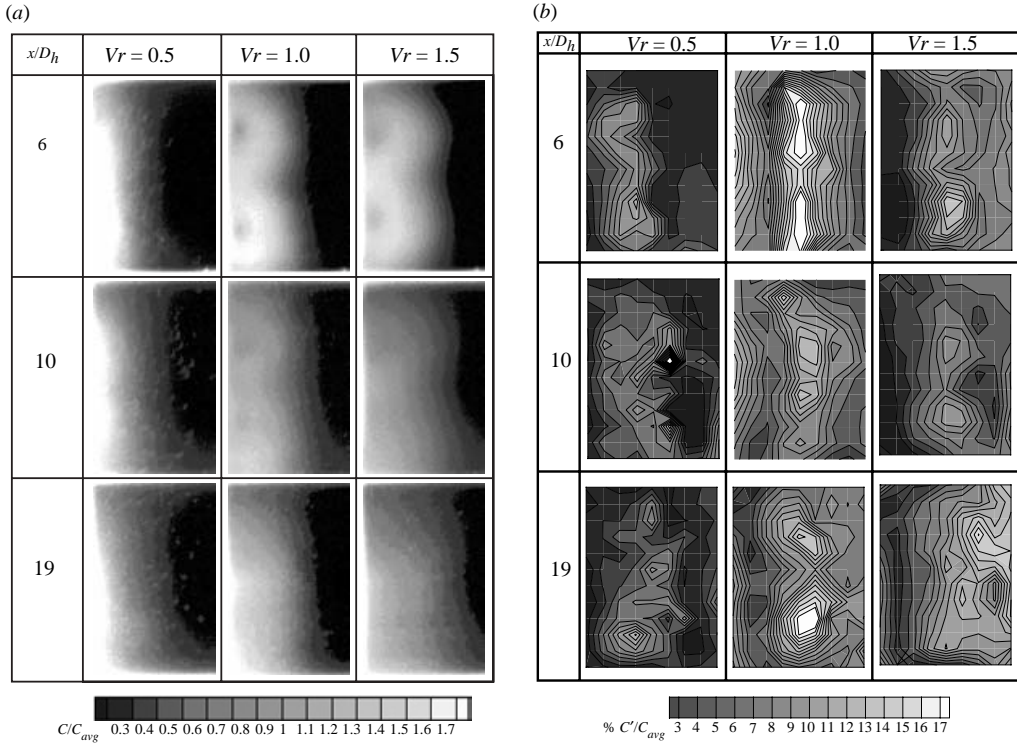


FIGURE 8. Composite (a) mean scalar concentration map and (b) concentration fluctuation map for $\alpha = 18^\circ$.

between the average concentration within the grid cells (approximately 2500 pixels). These data are not only averaged over the number of independent realizations taken over time, but also spatially averaged. A single interrogation region contains over 10 000 individual measurements. Estimated uncertainty in r.m.s. values is up to $\pm 15\%$, owing largely to the small ensemble size, which represented the optimal compromise between available run time, data storage and statistical convergence of the mean. Because of the spatial ‘binning’ followed by ensemble averaging, the estimate of 15% uncertainty was not determined by employing the classical analysis for a single random variable, but rather was based on a zeroth-order repeatability analysis. In this case, data sets were acquired under nominally the same conditions on different days and then processed in the same manner. The maximum differences between such sets of data were within the 15% uncertainty stated. Contour plots of mean and fluctuating concentration are grouped by injection angle in the subsequent figures. There are three columns corresponding to (from left to right) $Vr = 0.5, 1.0$ and 1.5 , and three rows corresponding to (from top to bottom) $x/D_h = 6, 10$ and 19 .

3.1.1. Results from $\alpha = 18^\circ$ and 24° cases

Figures 8(a) and 8(b) show representative shallow-angle results. The scalar concentration maps (SCM) and concentration fluctuation maps (CFM) each exhibit similar features for the 18° and 24° cases, so only the 18° results are presented. For $Vr = 0.5$, the jet fluid (marked with light regions) is immediately folded onto the injection wall by the crossflow. Hence, the injected scalar is confined to a thin layer along the injection wall (left-hand side of the image). There is little or no improvement in

mixing across the main duct as downstream distance increases, which will later be shown to indicate the weakness or absence of large-scale secondary-flow structures. This is reflected by the large persistent particle-lean areas (dark contours) on the right-hand side of the SCM, indicating that almost no jet fluid has penetrated into this region. The corresponding CFM plots for $Vr = 0.5$ (figure 8(b) first column) also show that there are no definable large-scale structures. This flow regime is the ideal configuration for film cooling applications where the coolant jet is intended to blanket the surface, protecting it from hot gases in the main stream.

Scalar concentration maps for $Vr = 1.0$ and 1.5 indicate the presence of the CRVP via circular grey regions with small dark centres (figure 8a). The CRVP is also obvious in the corresponding CFM (figure 8b), which shows two distinct regions of high-concentration fluctuations. These regions of high-concentration fluctuations do not coincide with the centres of the circular regions in the scalar field plots, but rather they coincide with the jet-crossflow interface shown in the SCM. In these shallow-angle cases, the CRVP is weak and located near the wall, so the strongest concentration fluctuations occur where the CRVP and shear-layer vortices displace the jet-crossflow boundary. Rathgerber & Becker (1983) also found that the highest-concentration fluctuations were coincident with the extremes of the jet, and that the CRVP cores were regions of minimum fluctuations.

The size and strength of the CRVP increases with increasing velocity ratio as reflected by the circular regions in the SCM (figure 8a top row, middle and right-most image). Mean velocity data confirm that these vortical structures are spatially stationary. It should be noted that ‘stationary’ does not mean non-moving in the strictest sense. The flow is expected to jitter about the mean jet trajectory. Despite the increased strength of the CRVP in the $Vr = 1.0$ and 1.5 cases compared to the $Vr = 0.5$ case, they experience little improvement in mixing across the duct, indicating that the cross-stream momentum of the jet is not sufficient to lift it off from the wall. The CFMs for $Vr = 1.0$ and 1.5 cases (figure 8b) show considerable differences between all the cases. Increasing velocity ratio causes the high-fluctuation regions to move further away from the injection wall. This is expected, as increasing velocity ratio improves jet penetration. Within the same velocity ratio cases, increasing downstream distance causes an increase in the size of the fluctuating regions. This is an indication of turbulent diffusion of the large-scale structures. Higher injection angles and velocity ratios cause the formation of stronger large-scale structures, which organize the secondary velocity field sooner, and make the effects of diffusion evident sooner.

3.1.2. Results from $\alpha = 30^\circ$ case

The 30° case bears similarity to the other low-angle cases, but also begins to exhibit a very different character, shown in figure 9(a) (lower right). At $Vr = 0.5$, the scalar field exhibits increased cross-stream penetration with downstream distance, as indicated by the displacement of the light/dark boundaries to the right. Mixing across the duct is considerably better at $x/D_h = 19$ compared to the shallower-angle cases, indicating that the flow field has entered a new regime. The existence of the CRVP is evident from the subtle curved double-humped shape of the particle-rich regions (e.g. figure 9a, middle-left). The corresponding CFM depicts patterns consistent with the presence of the CRVP (figure 9b). That is, the CRVP causes high-concentration fluctuations on either end of the kidney-shaped cross-section of the jet and lower fluctuations near the middle of the kidney (between the vortices). These signatures are very clear in the $Vr = 1.0$ and 1.5 cases. For the $Vr = 0.5$ case (figure 9b left column) a single dominant vortex appears to be oscillating up and down as it travels downstream. Note the

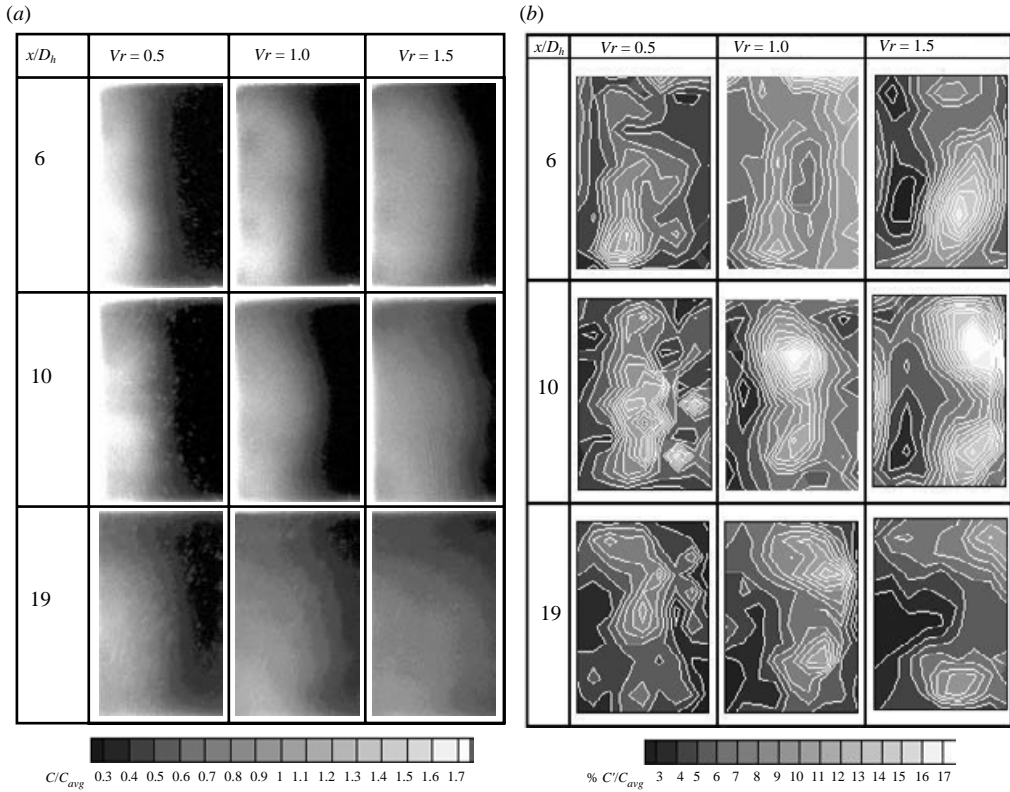


FIGURE 9. Composite (a) mean scalar concentration map and (b) concentration fluctuation map for $\alpha = 30^\circ$.

single region of high fluctuations (lighter regions) moves from the lower half of the duct at $x/D_h = 6$, to the middle of the duct at $x/D_h = 10$, and finally to the top half of the duct at $x/D_h = 19$.

The mean scalar concentration maps in figure 9(a) for $V_r = 1.0$ and 1.5 at $x/D_h = 6$ have the appearance of the corresponding figures in the shallower-angle case. At $x/D_h = 10$, the particle cloud marking the jet fluid (light regions) begins to be skewed towards the lower wall. At $x/D_h = 19$, the bulk of the tagged secondary duct (jet) fluid has moved to the injection wall–floor junction (lower left-hand corner of image). The evolution of the shapes of the particle cloud is not consistent with a continuing influence of two counter-rotating vortices of equal strength, but rather indicates the presence of one dominant vortical structure. One explanation is that the lower vortex is initially stronger than the upper one. This leads the upper vortex to move closer to the injection wall where it dissipates more rapidly, while the lower one is pushed away from the injection wall, resulting in better mixing in the lower portion of the duct. The velocity data to be presented will confirm this hypothesis. The CFM plots (figure 9b) also have similar features to those from the smaller angles. The major differences are that the fluctuating structures show more pronounced movement across the duct, as expected for a higher injection angle. The $V_r = 1.5$ case also shows another unusual characteristic: the formation of low-intensity fluctuating (dark) regions mirroring (left to right) the high fluctuating regions. These regions of low fluctuation correspond to the regions of high velocity, and are likely to be associated with the centres of the CRVP as found by Rathgerber & Becker (1983).

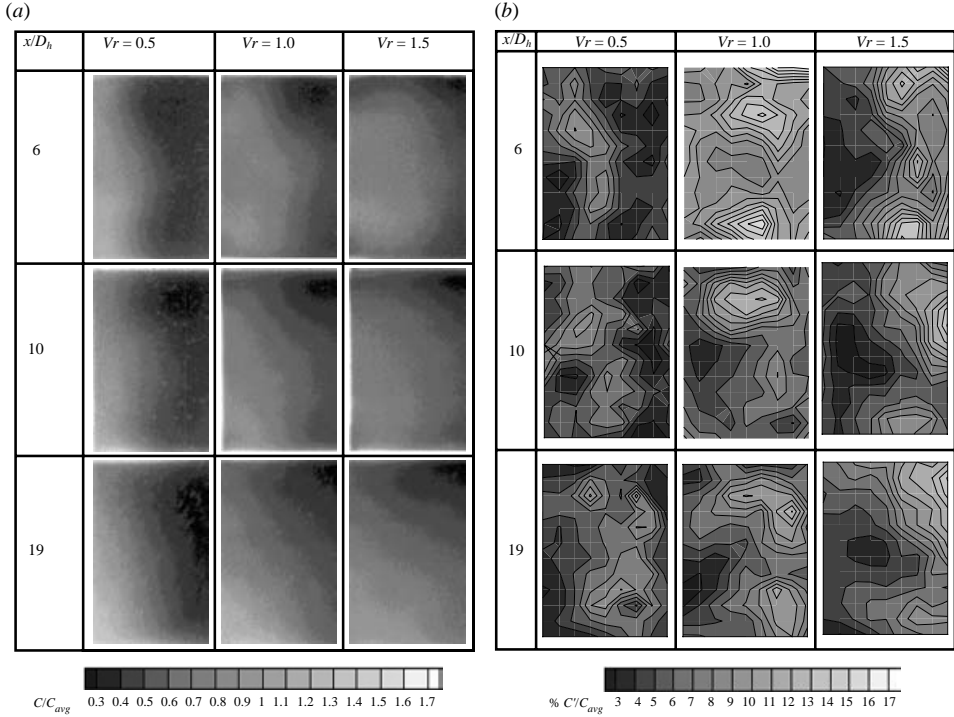


FIGURE 10. Composite (a) mean scalar concentration map and (b) concentration fluctuation map for $\alpha = 48^\circ$.

3.1.3. Results from $\alpha = 48^\circ$ case

The $Vr = 0.5$ SCM (figure 10a) show little evidence of large-scale mixing across the duct, suggesting wall-jet behaviour. At this low-velocity ratio, the CRVP is expected to be weak, resulting in little mixing. However, the CFM reveal organized regions of high fluctuation at all downstream locations, a signature of the CRVP. The existence of these organized regions at $x/D_h = 19$ (figure 10b lower-left) indicates that while weak, the CRVP persists far downstream. Combining the results of the SCM and the CFM leads to an important conclusion. The regions of high scalar concentration near the injection wall shown in the SCM and the coherent structures shown in the CFM, are indications that the jet can ‘reattach’ to the wall while still maintaining the CRVP downstream. This condition causes the scalar field to become better mixed with increasing downstream distance, in contrast to the wall jet behaviour documented in the 18° and 24° cases. A change in jet trajectory and wake structure is also observed in flow-visualization results, affirming that a new regime has been entered.

The $Vr = 1.0$ case (figure 10a middle column) reveals improvement in mixing, as depicted by the movement of the well-mixed (contour levels corresponding to 1) regions away from the injection wall. The bulge in the middle of the concentration map at $Vr = 0.5$ and $x/D_h = 6$ becomes much more pronounced at $Vr = 1.0$. This is caused by an increase in the strength of the CRVP and a corresponding increase in entrainment. The jet strongly interacts with the low-momentum fluid near the injection wall and the floor of the duct, as can be seen at $Vr = 1.0$ and $x/D_h = 19$ (migration of marked jet fluid to the lower left corner).

In the $Vr=1.5$ cases, the jet appears to be elevated or ‘lifted’ from the wall as particle-rich regions of the SCM depict the classical kidney-shaped cross-section for the first time (figure 10a top-right). The strength of the CRVP can be inferred from these images by the degree of change from one measurement location to another, as well as increase in the number of well-mixed areas in the planes of interrogation. The majority of entrainment in jet-in-crossflow occurs along the jet spanwise centreline on the injection side of the jet, where the CRVP acts to ‘pump’ crossflow fluid into the centre of the jet. Entrainment results in a locally well-mixed condition shown by regions of grey contours near the centre of SCM. The stronger the CRVP, the more fluid it entrains, and the more rapidly the (tagged) jet fluid is mixed out. The CRVP, for this case, is much stronger than in previously discussed cases, resulting in the large well-mixed regions at $x/D_h=6$ (figure 10a top-right). The region of high entrainment/CRVP strength is confirmed by velocity field results that show the rapid mixing of streamwise momentum (see §3.2). By the last measurement location, $x/D_h=19$, the flow is very well mixed across the entire duct, but asymmetric from top to bottom. A discussion of asymmetry is provided in §3.3.

3.1.4. Results from $\alpha = 60^\circ$ and 90° cases

The 60° and 90° cases exhibit lifted jet behaviour, resulting in substantial improvement in mixing as x/D_h is increased from 6 to 19 (figure 11a). There is, however, a dramatic departure from the patterns previously observed in the 48° case. As x/D_h increases from 10 to 19, a major change occurs in the SCM for both angles and all velocity ratios.

For the 60° case (not shown for brevity, see Cusano 1999), the particle-lean region moves from the right-hand side to the top of the scalar maps. This is an exaggeration of the behaviour of the 48° case and is consistent with a single large dominant vortex in the lower half of the duct. This is verified by the large low-fluctuating region found in the CFM for the 60° , $x/D_h=19$, and $Vr=0.5$ to 1.5 cases. Recall that the centre of a vortical structure is indicated by a minimum value in concentration fluctuation.

The 90° case at $x/D_h=19$ SCM (figure 11a bottom row) shows the low-concentration region in the geometric centre of the duct instead of at the top as in the 60° case. The CFM (figure 11b) is similar to those of previously described cases at $x/D_h=10$ (middle row), but the high-fluctuation regions become disorganized and show an overall decrease in magnitude at $x/D_h=19$ (bottom row). These SCM and CFM imply that the organized structure of the jet is severely weakened or destroyed between $x/D_h=10$ and $x/D_h=19$. The $x/D_h=19$ SCM represent the best mixed of all cases, as they show results similar to a far-field mixing case. The other obvious difference found in the 90° case is the concave shape (concave going from the particle-lean to particle-rich regions, i.e. light to dark contours) in the jet mixing boundary in the SCM at all conditions, versus the other convex shape found at other injection angles. One explanation for this is that under these circumstances the jet experiences a separation on the upstream wall of the secondary duct. Maximum separation is expected at the jet (spanwise) centreline, forming a half-elliptical-shaped separation region, which attaches at the corners of the secondary duct. Flow visualization supports this hypothesis (see Cusano 1999).

3.2. Velocity fields

Two velocity ratios ($Vr=1.0, 1.5$), six downstream distances ($x/D_h=3, 6, 10, 15, 19, 40$) and two injection angles ($\alpha=30^\circ, 48^\circ$) were investigated in a full factorial test matrix yielding 24 experiments. To document inlet conditions, velocity field data

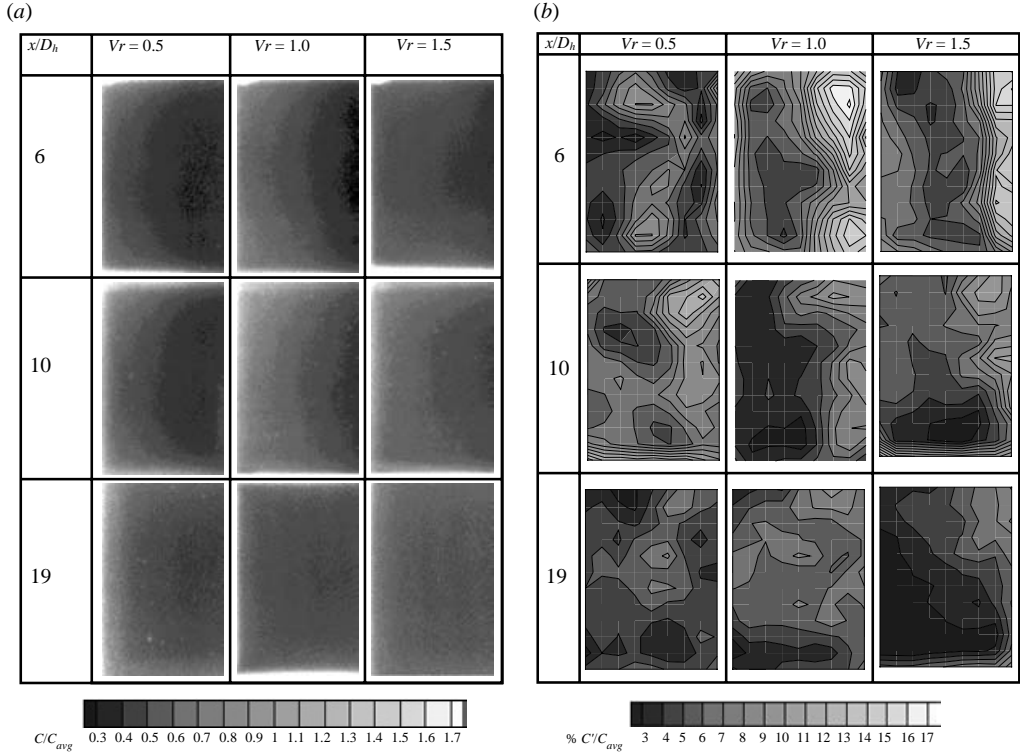


FIGURE 11. Composite (a) mean scalar concentration map and (b) concentration fluctuation map for $\alpha = 90^\circ$.

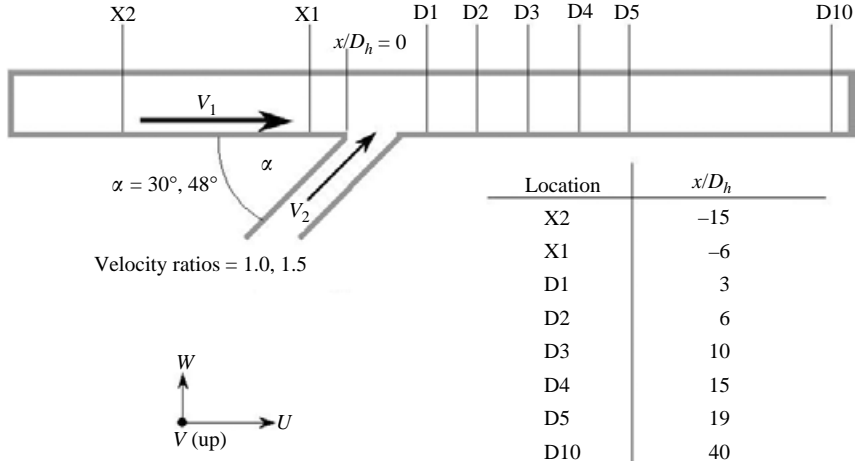


FIGURE 12. LDV measurement locations.

were obtained at two stations (upstream of the intersection) in the main duct and at one station in the secondary duct (see figure 12). Measured velocities in the main duct are presented in the form of contour plots for the mean streamwise U component normalized by the average (U_{avg}) velocity over an entire grid, overlaid with two-dimensional secondary flow vectors created from the V and W components. The

results for the $Vr = 1.5$ case will be discussed in detail. The $Vr = 1$ data are discussed later and shown in figures 16 and 17.

3.2.1. $Vr = 1.5$, $\alpha = 30^\circ$, mean velocity field

The jet can clearly be seen as the light contour region with high mean streamwise velocity (U) at $x/D_h = 3$ (figure 13a). Note that the contours in this series of plots correspond to streamwise velocity magnitude, not concentration. The secondary velocity vectors indicate that there is a significant blockage caused by the jet, as the crossflow negotiates around the blockage created by the jet. Note that the secondary velocity field (vector arrows) is fairly uniform within and between the jet and the crossflow. This indicates that the jet and crossflow fluids are travelling nearly parallel to each other as the jet is penetrating into the crossflow. For the corresponding $Vr = 1$ case, there was little evidence of the jet in the mean streamwise velocity field. However, the jet blockage was manifested in a similar but weaker secondary velocity field.

At $x/D_h = 6$ the mean velocity field is changed considerably, as the action of the CRVP dominates the flow field. Characterizing the action of the CRVP by considering its effect on jet entrainment is useful. The middle of the flow field shows no indication of the high-velocity jet fluid. Entrainment has already mixed out the higher streamwise momentum of the jet (see figure 13b). This leaves two cores of high-velocity jet fluid (indicated by the light contours), which generally correspond with the centres of the CRVP. Fluid within the CRVP cores is not mixed with the lower-velocity fluid outside the structures.

Velocity vectors normal to the interface between the two streams (shear layer) result in efficient mixing of momentum. The action of the CRVP induces a velocity field tangent to the fluid shear layer, slowing the mixing process. As downstream distance increases, the secondary velocity field associated with the CRVP weakens (the vortices grow in size as a consequence of diffusion and conservation of angular momentum), resulting in the gradual mixing out of the high-momentum cores, as seen at $x/D_h = 10$ to 19 (figure 13c–e). Note that the centre of the upper vortex, as shown in the secondary velocity field vectors, coincides with the local region of high streamwise velocity. However, the lower vortex does not. This is atypical of the expected CRVP development and is possibly caused by the main flow negotiating the jet asymmetrically and exacerbated by the confinement. This is further discussed in § 4.1.

3.2.2. $Vr = 1.5$, $\alpha = 48^\circ$, mean velocity field

This case exhibits a high degree of entrainment, even at the first measurement location, $x/D_h = 3$. The jet core is already split into the two-core structure with an extremely strong low-momentum region in the centre. This low-momentum region can be characterized as the ‘wake’ of the jet, or as a separation bubble. This region contains reversed flows (negative U) measured at points adjacent to the wall (this is obscured by the choice of contours of figure 14). By $x/D_h = 6$, the strong entrainment has created a large low-momentum region in the centre of the duct. The twin jet core is still evident, but much weaker than in the 30° case. At positions $x/D_h = 15$ and $x/D_h = 19$, the strong pumping action of the CRVP and the associated high level of entrainment are again evident. The far-downstream condition, $x/D_h = 40$, shows the streamwise velocity field had nearly returned to the fully developed distribution measured upstream of the intersection. The effects of the CRVP are still evident in the secondary flow field as shown by their magnitude and organization of the velocity vectors.

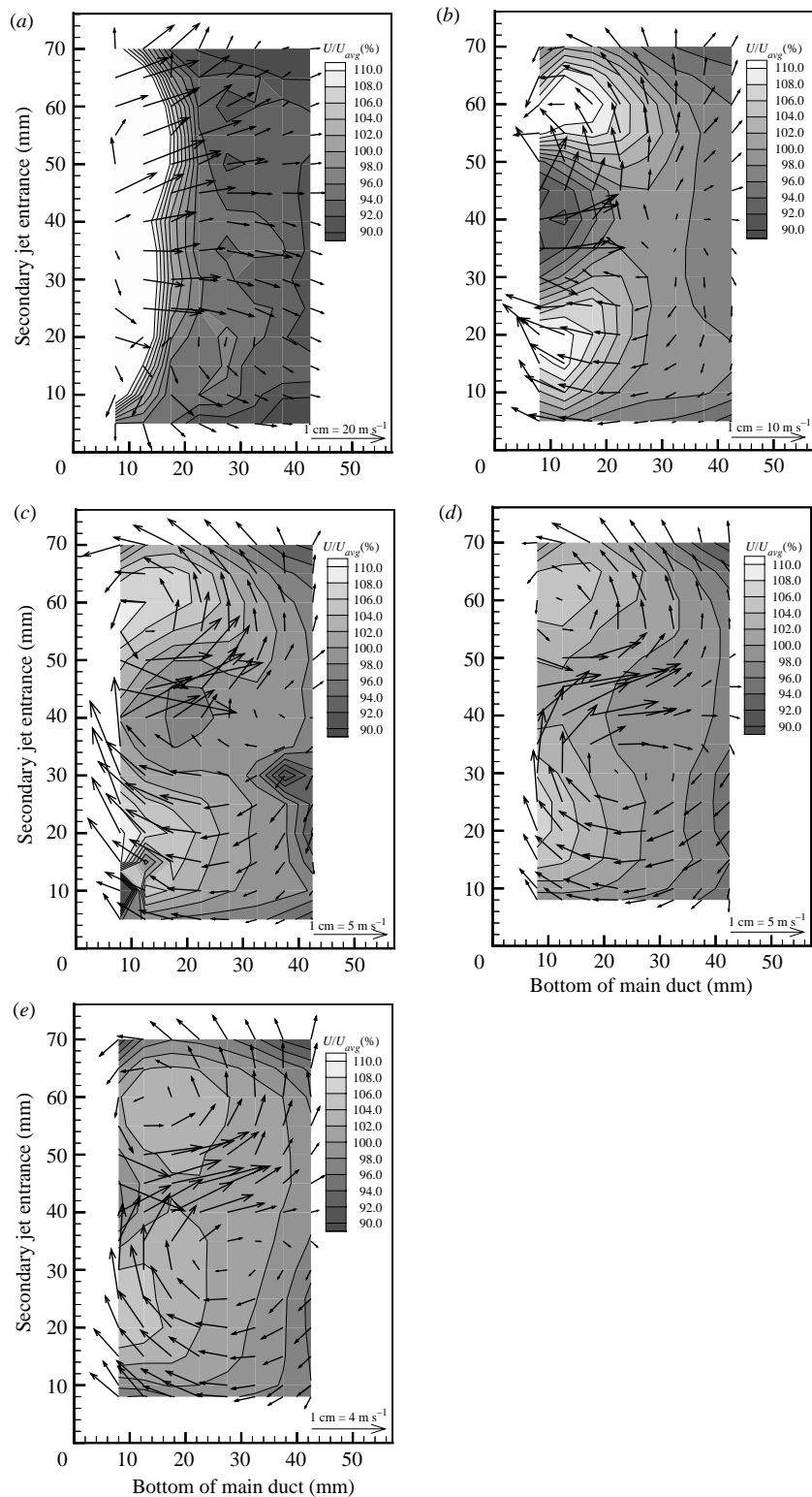


FIGURE 13. Three-dimensional mean velocity field development: $\alpha = 30^\circ$, $Vr = 1.5$.
 (a) $x/D_h = 3$, (b) 6, (c) 10, (d) 15, (e) 19.

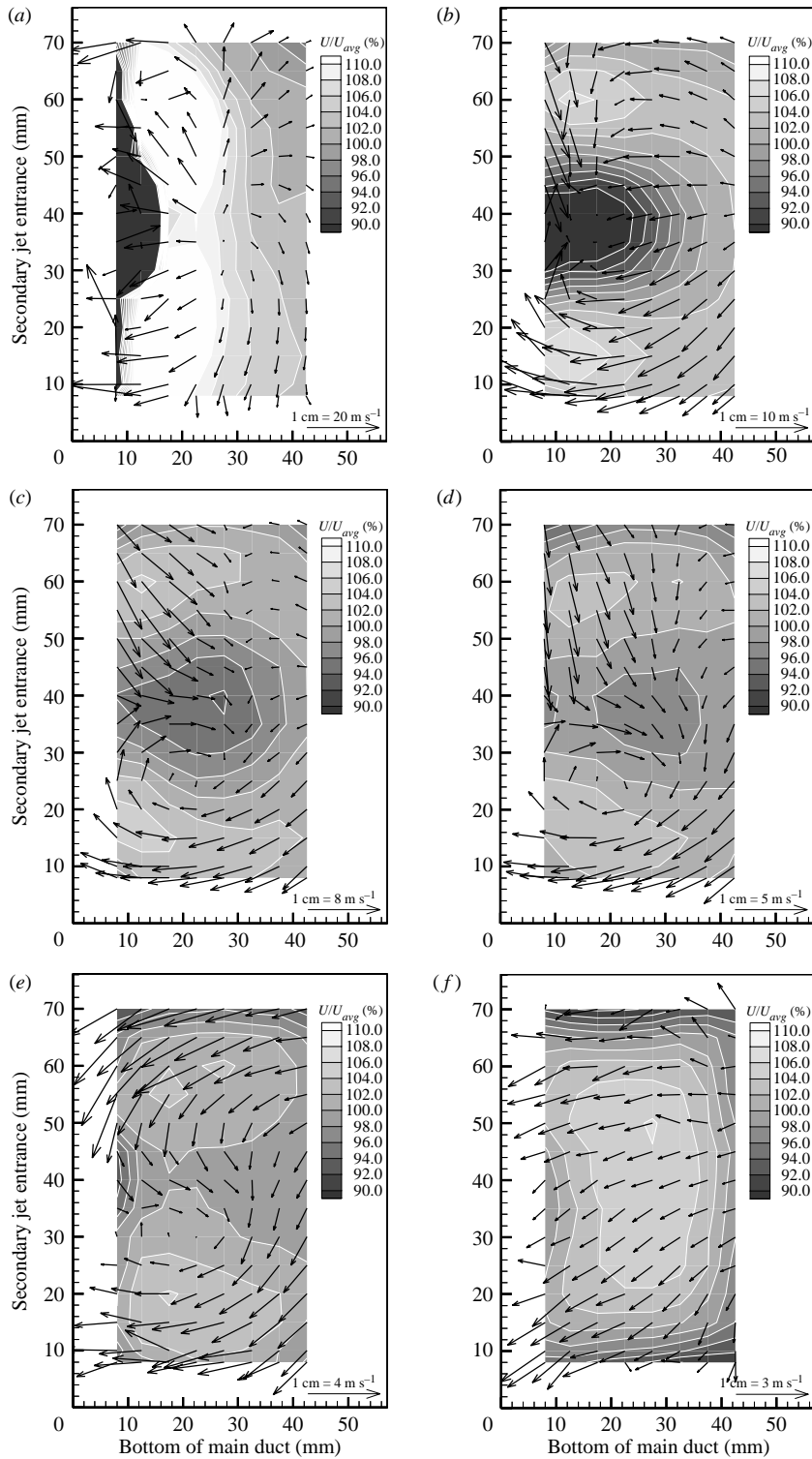


FIGURE 14. Three-dimensional mean velocity field development: $\alpha = 48^\circ$, $Vr = 1.5$.
 (a) $x/D_h = 3$, (b) 6, (c) 10, (d) 15, (e) 19, (f) 40.

Asymmetry at 48° is evident at both velocity ratios, but as in the 30° case the effects vary. At $Vr = 1.0$ (see figure 17), the secondary velocity field is symmetric (within the error bounds of the experiment), while the high streamwise velocity core of the main duct is biased towards the lower half of the duct. For $Vr = 1.5$, the velocity core exhibits similar behaviour, but the secondary velocity field has marked asymmetry both in magnitude and direction. The secondary velocity vectors indicate a very strong lower vortex and an apparent absence of the upper one.

3.2.3. Velocity maximum

Previous workers have linked the location of maximum streamwise velocity to the location of the centres of the counter-rotating vortices. In addition to the loci of maximum velocity, the rate of its decay is also of interest. Both factors are important to the mixing process. Figure 15 shows the location of maximum velocity (triangle symbols) and its magnitude (square symbols) for $Vr = 1.0$ and 1.5 and $\alpha = 30^\circ$ and 48° , for $3 \leq x/D_h \leq 19$. The numbers 1 to 5 correspond to the measurement location (e.g. '1' indicates location D1) as illustrated in figure 12. There is a markedly different character between the results for the two velocity ratio cases in the plots. This difference is attributable to the differences in the jet velocity signature, as described in the previous sections and reviewed below.

All of the $Vr = 1$ cases have a single region of high velocity located across from the injection wall. The crossflow and jet have the same bulk speed at $Vr = 1$, but because the jet is injected at an angle its streamwise velocity component is less than that of the crossflow. Thus, the positions of maximum velocity plotted in figures 15(a) and 15(c) delineate the region where the maximum speed of the crossflow accelerating around the jet is located. On the other hand, for $Vr = 1.5$, the regions of maximum velocity are associated with the jet fluid and thus should mark the location of the vortices. Recall that the strong entrainment associated with $Vr = 1.5$ causes the spanwise centre of the jet to mix out, leaving two high-speed jet cores. In figure 15(b) and 15(d), the dashed lines correspond to the upper vortex and the solid lines to the lower vortex.

In all of the $Vr = 1.0$ cases (figure 15a, c) the location of the maximum velocity region (triangles) progresses downward for the first three measurement locations, then oscillates across the main duct. This corresponds to the asymmetry in the mixing field (top to bottom), i.e. higher scalar concentration is biased toward the bottom of the duct. For $Vr = 1.5$ (figure 15b, d), an interesting phenomenon is observed for both angles. The maximum velocity regions corresponding to the CRVP appear to move in a circular fashion in the same direction as the vortex-induced flow. That is, the upper vortices move counterclockwise and the lower vortices move clockwise. Thus, the vortices appear to be spiralling downstream.

Velocity decay lines (squares) also reveal some interesting trends. For the 30° , $Vr = 1.5$ case (figure 15b), the upper and lower regions of maximum velocity are nearly equal in magnitude over the range of downstream distances. When the angle is increased to 48° , figure 15(d) shows that the maximum velocity associated with the lower vortex (solid line) is initially much lower at $x/D_h = 3$ (D1) than that associated with the upper vortex (dashed line). However, velocity magnitudes associated with the upper and lower vortices are nearly equal for all downstream stations.

Comparing the $Vr = 1.0$ cases (figure 15a, c), maximum velocity is initially nearly identical for both angle cases. The $Vr = 1.0$, 48° case maximum velocity decays in a nearly linear fashion, whereas that for the 30° case decreases linearly, but then increases downstream of $x/D_h = 10$ (D3). This can be explained by recalling that for the low-angle case, the secondary jet has not penetrated far into the flow. By $x/D_h = 15$

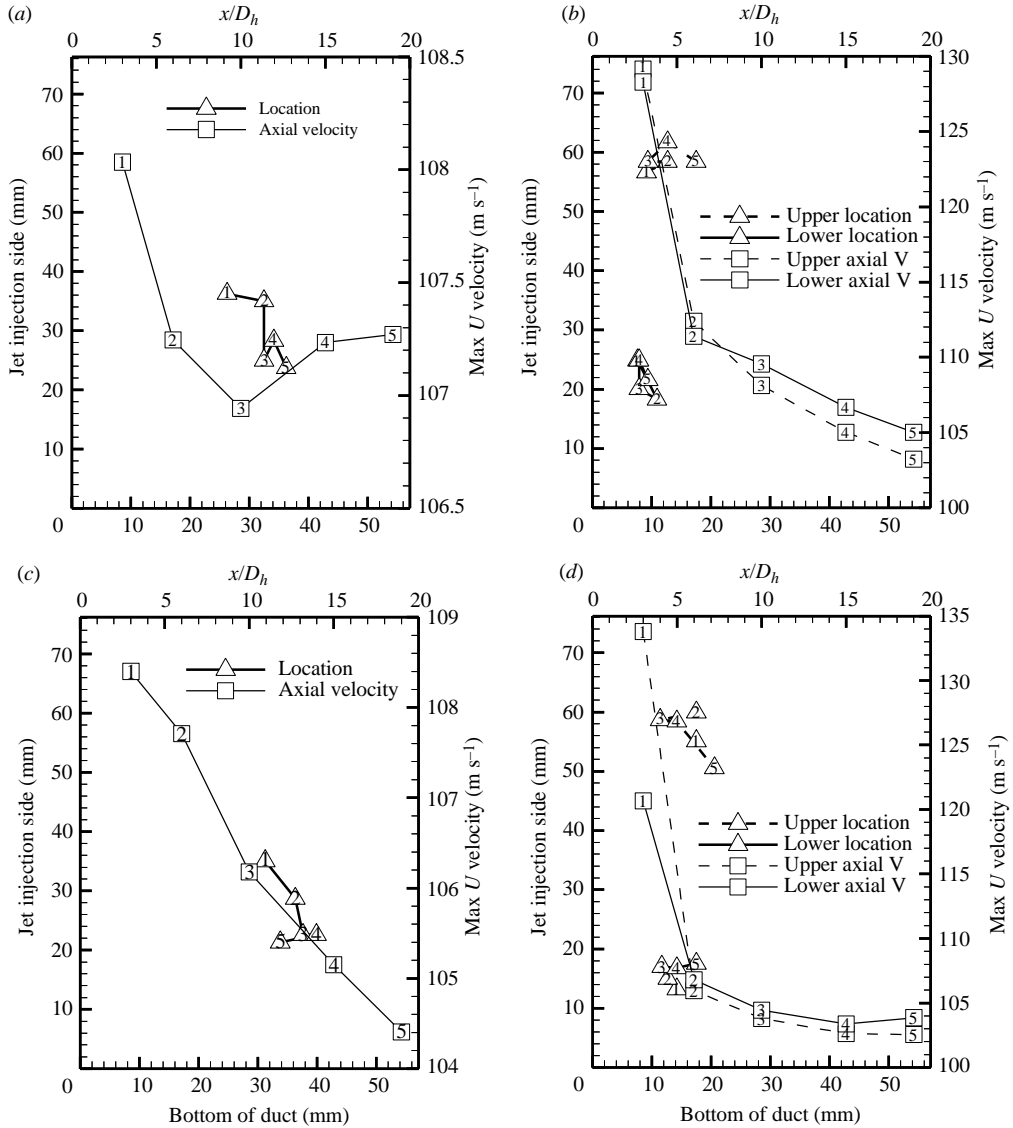


FIGURE 15. Location and magnitude of maximum velocity for $x/D_h = 3-19$. (a) $30^\circ - Vr = 1.0$, (b) $30^\circ - Vr = 1.5$, (c) $48^\circ - Vr = 1.0$, (d) $48^\circ - Vr = 1.5$.

(D4) the low-momentum fluid of the jet and the CRVP has moved far enough across the duct to create a blockage, reduce the effective area of the main duct and ‘squeeze’ the crossflow, causing the slight increase in maximum velocity. When the injection angle increases to 48° , the crossflow and jet flows interact in a more three-dimensional fashion (flow is no longer in the ‘wall jet’ regime) and the velocity decays very rapidly, as discussed earlier for normal injection case.

3.3. Asymmetry investigation

An asymmetry in the mean scalar concentration distribution is evident in the data over a wide range of parameters. The particle-lean region located at the top right-hand corner of the composite images characterizes the scalar field asymmetry. In particular,

the asymmetry was most pronounced for injection angles greater than 30° , as well as some velocity ratios and downstream locations in the 30° case. The corresponding secondary velocity field also exhibits asymmetry in the size and position of the CRVP. While there are documented cases of asymmetry in symmetric flows, an investigation was required to verify that these results were not a consequence of an experimental anomaly.

Several hypotheses for the cause of the asymmetry were formulated: (i) settling or clumping of seed particles; (ii) experimental error in the planar mixing diagnostics system; (iii) flow disturbance or a geometric anomaly; (iv) contaminated initial conditions; and (v) naturally-occurring asymmetry, perhaps driven by an instability mechanism. All of these hypotheses were evaluated (Cusano 1999). A few highlights are given below.

Particle settling was dismissed because of the high convection velocities of the flow compared to the particle settling time under the action of gravity. For example, an aluminium oxide seed particle with a convection velocity of 80 m s^{-1} will fall approximately 1 mm ($< 1.5\%$ of the duct height) over the approximately 1 m length from the point of injection to $x/D_h = 19$ station. Experimental error associated with the scalar measurement technique was also eliminated as a possible explanation because of the corresponding asymmetric flow structures found in the velocity data. These velocity data were acquired by an entirely different technique, with different seeding, different measurement times and sample sizes, almost a year after the scalar concentration data. The excellent correspondence of these two data sets cannot be coincidental, and thus eliminates the experimental error hypothesis.

An imperceptible geometric anomaly in the test rig or irregularity in the flow delivery system could potentially produce contaminated initial conditions. However, the inlet velocity field was verified to be symmetric in all measurable respects (Cusano 1999). The static pressure distributions were measured in the main duct (Yi & Plesniak 2002) to determine whether pressure non-uniformities could be correlated to the observed asymmetries. The total and static pressure distributions (20 points distributed across the cross-section of the main duct) at the inlet ($x/D_h = -52$) and the outlet ($x/D_h = 42$) of the test section were measured using a Pitot-static pressure probe and manometer. For $Vr = 0.5$ and $\alpha = 24^\circ$, the distributions of the total and static pressures varied less than 2% over the entire cross-sections. The deviations of the static pressures from the mean were 0.5% and 1.8% at the inlet and outlet, respectively. No systematic patterns in the pressure could be correlated to the asymmetric scalar concentrations and flow structures. Various imposed perturbations, including skew angle, wall roughness, flipped test section, asymmetric gap at the top and bottom, etc. were investigated and eliminated as sources of the asymmetry. The remaining hypotheses that asymmetry is a natural state for this flow, perhaps induced by an instability mechanism, could not be verified nor rejected. In light of the results reported by Smith & Mungal (1998) and Kuzo (1995), this remains a leading candidate for the asymmetry.

3.4. Summary

The results presented in this section are summarized as follows:

(i) Three distinct flow regimes were identified by analysis of the mean scalar concentration field, velocity field and flow visualization data. These are the ‘wall jet’, ‘reattached jet’ and ‘lifted jet’ regimes.

(ii) The rapid mixing made possible by the action of the CRVP occurs within $x/D = 10$, after which the flow structures gradually relax to the far-field condition.

(iii) The flow field develops asymmetrically, based on scalar concentration and velocity data, in planes normal to the bulk-flow direction.

(iv) The crossflow preferentially negotiates the blockage caused by the jet flow through the lower half of the main duct.

(v) Increasing velocity ratio (Vr) results in increased CRVP strength, increased jet penetration, increased jet entrainment, improved mixing and increased flow asymmetry.

(vi) The persistent CRVP influences the secondary velocity field throughout the main duct, $x/D = 40$.

(vii) The counter-rotating vortices appear to follow spiral paths as they progress downstream. The induced velocity field governs the direction of the spiral.

4. Discussion of results

The velocity field evolution is further examined. All three components of velocity at all streamwise locations are plotted together in three-dimensional plots showing a perspective of the JICF velocity field evolution. Considerable insight about the flow field can be gained by combining velocity and scalar field data and analysing the results. The first set of overlays to be presented consists of the scalar concentration field and the secondary velocity vector field data. Next, concentration fluctuation field data are combined with the secondary velocity vector field data. All of these plots are made for the data locations common to both LDV and concentration data sets ($\alpha = 30^\circ$ and 48° , $Vr = 1.0$ and 1.5 , and $x/D_h = 6, 10$, and 19). Finally in this section, schematics of the jet/crossflow interaction and a regime map describing the character of the JICF are presented.

4.1. Three-dimensional mean velocity field evolution

Figures 16 and 17 show the overall three-dimensional mean velocity field development. Detailed explanations of the flow field were given previously; however, with the new viewpoint, additional comments will be made. The streamwise evolution of the mean velocity field is presented in a three-dimensional display format, with secondary velocity vectors overlaid on streamwise velocity contours.

Comparing figures 16 and 17, the effect of increasing the injection angle from 30° to 48° on the mean velocity field is apparent immediately at $x/D_h = 3$, where there was a well-defined low-momentum region corresponding to the jet (black area near the injection wall) for the 48° case. Here, the secondary velocity field indicates no migration of jet fluid away from the injection wall. One possible explanation is that the steeper injection angle causes the flow to penetrate further into the crossflow than for the shallower-angle cases, but because of the low velocity ratio, the jet is completely bent-over by the time it reaches the first measurement station. This explains the near-zero magnitude velocity vectors in the centre of the duct. Other trends are the same as observed in the 30° angle case, except that the entrainment appears to be much stronger, as indicated by the size and growth of the low-momentum region.

Increasing the injection angle from 30° to 48° results in a halving of the streamwise distance required to achieve a similar level of flow interaction and large-scale mixing. Data were also collected at a far downstream ($x/D_h = 40$) location for the 48° case, for which the streamwise velocity component had nearly returned to the distribution measured upstream of the intersection. The secondary flow field, on the other hand, showed velocity vectors similar to those at $x/D_h = 19$, only weaker. This is an indicator that the structures causing the velocity distributions at $x/D_h = 3$ to 19 exist at least

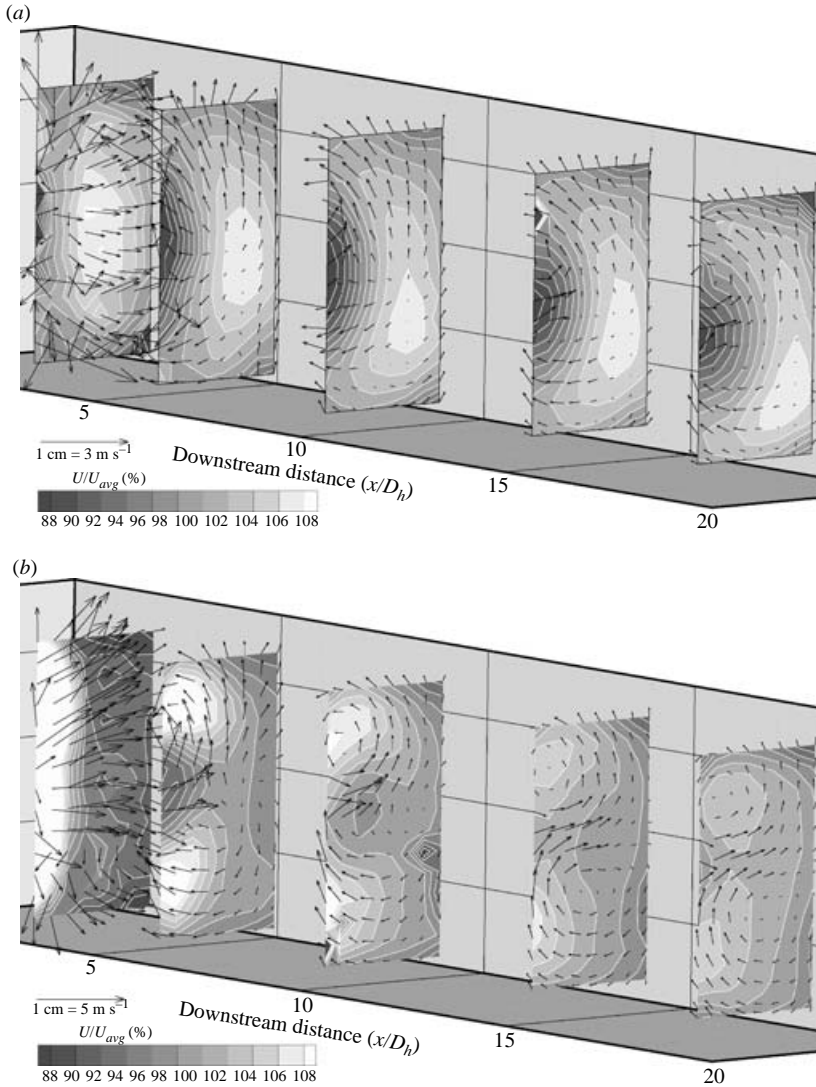


FIGURE 16. Streamwise development of mean velocity field for $\alpha = 30^\circ$, and (a) $Vr = 1.0$, (b) $Vr = 1.5$.

up to $x/D_h = 40$, consistent with the persistent nature of the CRVP reported by Rathgeber & Becker (1983).

Figure 16(a) highlights the difference in the streamwise distance required for the various velocity components mix out. The large secondary velocities present at $x/D_h = 3$ decay until $x/D_h = 10$, when they seem to reach asymptotic values. This supports the assertion that the region of rapid mixing occurs for $x/D_h < 10$. However, the streamwise velocity field behaves much more monotonically.

Figure 16(b) shows an entirely different behaviour compared to figure 16(a), and is representative of velocity ratios greater than 1.0. The secondary velocity field changes character in dramatic fashion between $x/D_h = 3$ and 6. At $x/D_h = 3$, the jet is well organized and penetrating towards the wall opposite to the injection wall. Within the next $3D_h$ the vortex structure forms and aggressively mixes out the streamwise

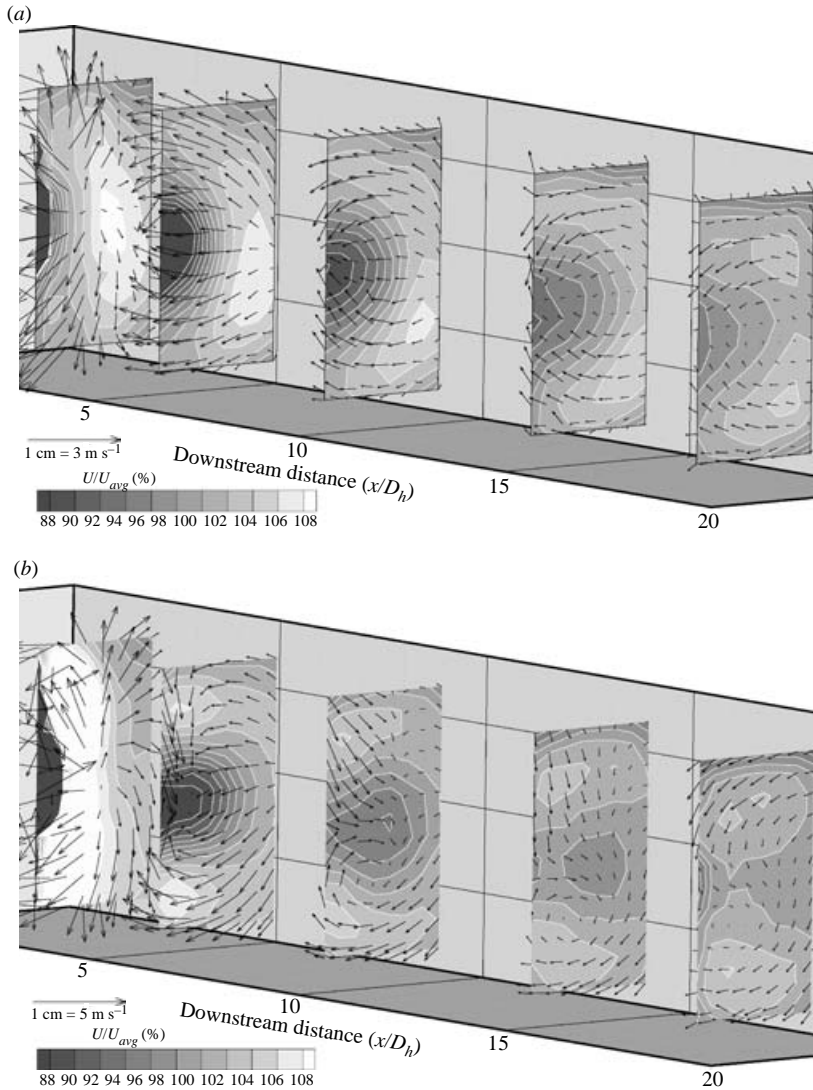


FIGURE 17. Streamwise development of mean velocity field for $\alpha = 48^\circ$, and (a) $Vr = 1.0$, (b) $Vr = 1.5$.

momentum of the jet between the CRVP structures. The vectors near the bottom of the main duct sweep towards the injection wall strongly, compared with the vectors near the top. As in the $Vr = 1.0$ case, the secondary velocity field undergoes little change after $x/D_h = 10$.

The $\alpha = 48^\circ$, $Vr = 1.0$ case (figure 17a) demonstrates that the crossflow negotiating the blockage of the jet, does not always occur in a symmetric fashion. Most of the main flow bypasses on the outboard side of the jet, more or less uniformly from the top to bottom of the duct, as shown in figure 18. At $x/D_h = 3$, the secondary velocity vectors are well organized in a downward sweep. Considering this, it is not surprising that the core of high crossflow velocity migrates to the bottom half of the duct, as shown at subsequent measurement locations.

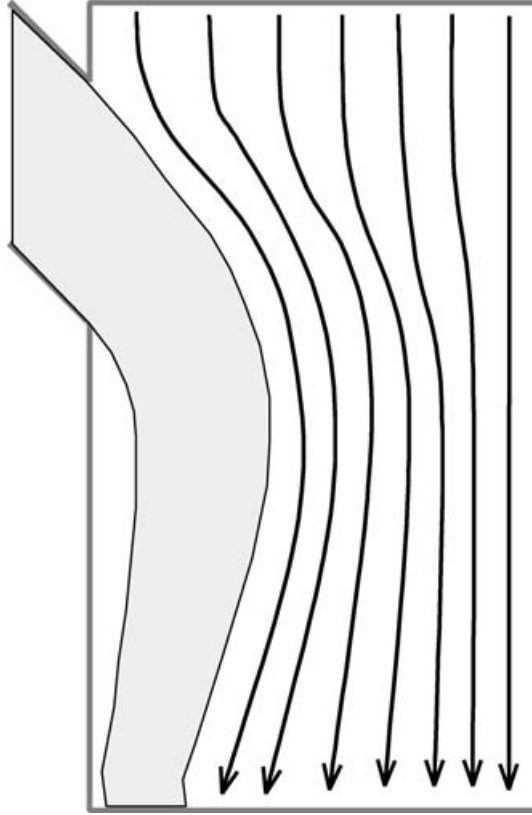


FIGURE 18. Schematic of crossflow-jet interaction for $\alpha = 48^\circ$, $Vr = 1.0$. Plan view.

Figure 17(b) also clearly shows the asymmetry of the crossflow negotiating the blockage caused by the jet. When the blockage is high (larger angles and velocity ratios), the main flow goes around the jet through the small gap at the top and bottom, as well outboard of penetrating jet. This interaction is shown schematically in figure 19, from a perspective view and a plan view. This should be contrasted to figure 18, which shows a more two-dimensional path of the crossflow around the jet when the blockage is small. Referring back to figure 17(b), at $x/D_h = 3$, there are strong secondary motions sweeping down and inward, as well as up and outward. Despite these strong motions, the same general behaviour as that exhibited by the $\alpha = 30^\circ$, $Vr = 1.0$ case occurs. The velocity field rapidly changes, reaching a somewhat ‘steady-state’ value by $x/D_h = 10$.

4.2. Scalar concentration and secondary velocity vector overlays

The scalar concentration field and secondary velocity vector field overlays relate the flow structures to their scalar field signatures and emphasize the effects of the parameters varied in the study. At $\alpha = 30^\circ$, $Vr = 1.0$ and $x/D_h = 6$ (figure 20a), the secondary velocity vectors demonstrate excellent correlation to the jet-crossflow interface shown by the concentration map. The secondary velocity vectors are aligned with the interface, indicating very little jet-crossflow mixing (no transport across the interface). The high-concentration region in the lower left-hand side of the duct corresponds to a region in the secondary velocity field consistent with that induced by a streamwise vortex. Moving to $x/D_h = 10$ (figure 20a), it becomes clear that the highest levels

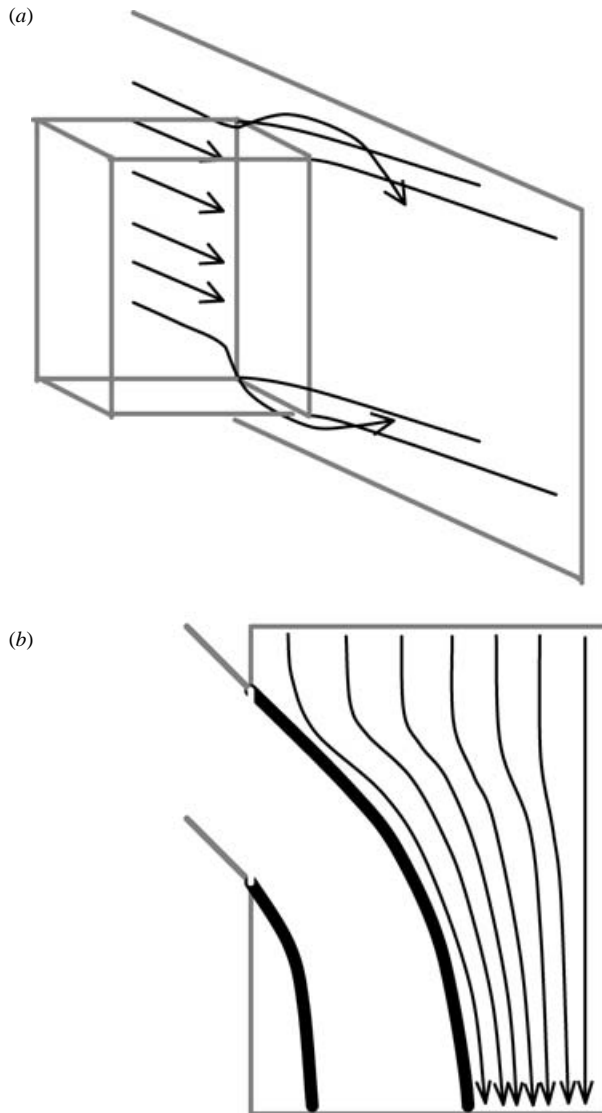


FIGURE 19. Schematic of crossflow-jet interaction for $\alpha = 48^\circ$, $Vr = 1.5$. (a) Perspective view. (b) Plan view.

of mixing occur where the secondary velocity vectors have the largest component normal to the concentration contour lines. Wherever the secondary velocity vectors are nearly zero or are oriented tangentially to the concentration contours, subsequent downstream locations experience only a marginal improvement in mixing with little or no movement of the mixing interface (darker grey contours, e.g. figure 20a centre of duct). Where the secondary velocity vectors are perpendicular to the concentration contours, subsequent SCM images show a dramatic movement (dependent on the magnitude of the secondary velocity) in the mixing interface and a corresponding improvement in the extent of mixing in that area. The secondary velocity field can thus be used to predict the behaviour of the mixing field at subsequent downstream locations. Finally, at $x/D_h = 19$, a clearly identifiable pair of counter-rotating vortices

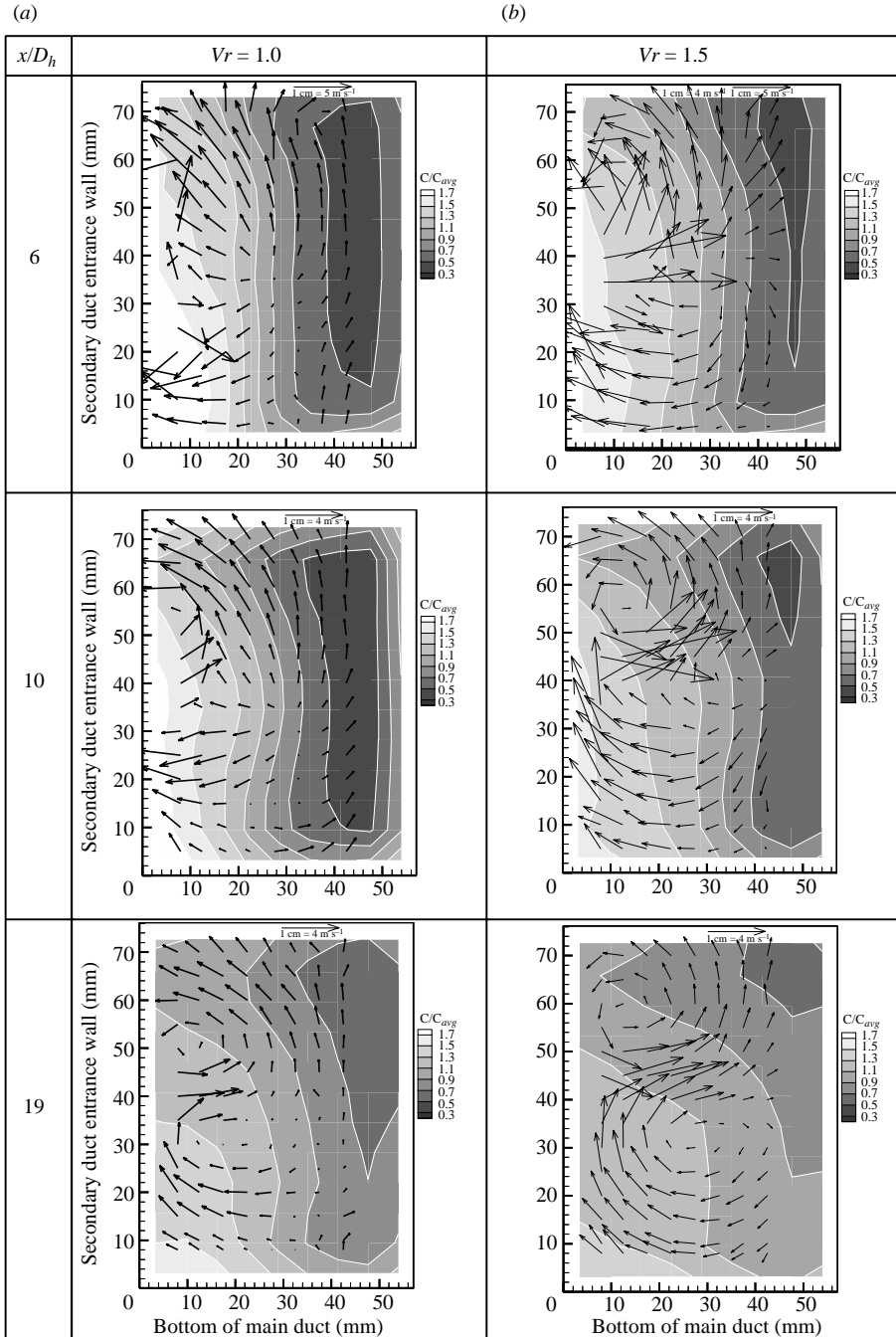


FIGURE 20. Mean scalar concentration-velocity field overlay and effect of development length, $\alpha = 30^\circ$, and (a) $Vr = 1.0$, (b) $Vr = 1.5$.

is observed. The vortices are asymmetric in size and location, and correspond well with the asymmetry in the concentration field. That is, the size and location of the well-mixed areas closely match the size and organization of the counter-rotating

vortices. This correlation between the secondary velocity field and the mixing images is not serendipitous given that data sets were taken more than a year apart.

For $\alpha = 30^\circ$, $Vr = 1.5$ (figure 20*b*), the secondary velocity field is considerably stronger than the $Vr = 1.0$ case (corresponding parts of figure 20*a, b* are plotted to the same scale and can be compared directly). At $x/D_h = 6$, the jet is still penetrating into the crossflow, signified by the secondary velocity vectors pointing away from the jet injection wall. The SCM shows a slight asymmetry coinciding with a strong tightly wrapped streamwise vortex flow in the upper left-hand corner. By $x/D_h = 10$, the vortex is more clearly evident, while a strong sweeping motion occurs in the lower half of the duct. The secondary velocity vectors in the lower half of the duct are aligned normal to the concentration contour lines, and predict the greatly improved mixing shown at $x/D_h = 19$. The sweeping motion observed at $x/D_h = 10$ develops into a large vortical structure (with nearly circular streamlines) at this location. The vortex pair shown in the lower part of figure 20(*b*) is asymmetric in size, location and strength, with the upper one being smaller and weaker, and offset to the jet-injection-side upper corner.

Comparing the previous two figures shows that the main effect of a higher velocity ratio is greater penetration across the duct and stronger CRVP. Low velocity ratios result in a more two-dimensional interaction between the jet and the crossflow, i.e. the main flow bypasses primarily around the right-hand side of the jet rather than at the top and bottom gap. The jet penetrates into the crossflow and is gradually bent back to the injection wall, as indicated by the secondary velocity vectors pointing towards the injection wall at $x/D_h = 6$. In the $Vr = 1.5$ case at this location, the vectors form circular streamlines, verifying the presence of a strong CRVP.

The character of the velocity and scalar fields is dramatically different for $\alpha = 48^\circ$, $Vr = 1.0$ (figure 21*a*). At each streamwise location the secondary velocity vectors all point towards the injection wall. It is hypothesized that the increased blockage causes a squeezing of the crossflow by the jet flow near the point of intersection. After injection, and subsequent realigning of the jet flow, the blockage is relaxed, causing the flow to move back towards the injection wall (this was depicted schematically in figure 18). The area near the injection wall beneath the jet is a low-pressure region. At $x/D_h = 6$, the velocity vectors are approximately of equal magnitude from the top of the duct to the bottom and increase in magnitude from the right-hand to the left-hand side of the duct. At the centre of the duct on the injection sidewall, the nearby vectors begin to take on a more vertical orientation and point towards the centre. By $x/D_h = 19$, the vectors along the vertical centreline of the duct and close to the top and bottom walls are nearly zero. As in the previous two cases, the velocity vectors oriented perpendicular to the concentration contours correctly identify where maximum mixing is occurring.

The velocity field again changes again for $\alpha = 48^\circ$, $Vr = 1.5$ (figure 21*b*). At $x/D_h = 6$, the velocity field is similar to that shown in figure 20(*b*), except for the region located above the vertical centreline next to the injection wall. In this area, the vectors point downward. As the flow progresses downstream and reaches $x/D_h = 10$, the vectors pointing towards the injection wall near the bottom of the duct remain strong and the vectors oriented towards the centre of the duct change direction and point towards the lower right-hand corner of the duct. A vortex appears in the lower half of the duct and the strong vectors along the bottom and top left of the duct appears to 'feed into' the structure. This single vortex structure is centred in the particle-rich region of the duct and corresponds to an asymmetric distribution of the scalar concentration field. The single-vortex condition persists to the $x/D_h = 19$ location, but a change occurs in

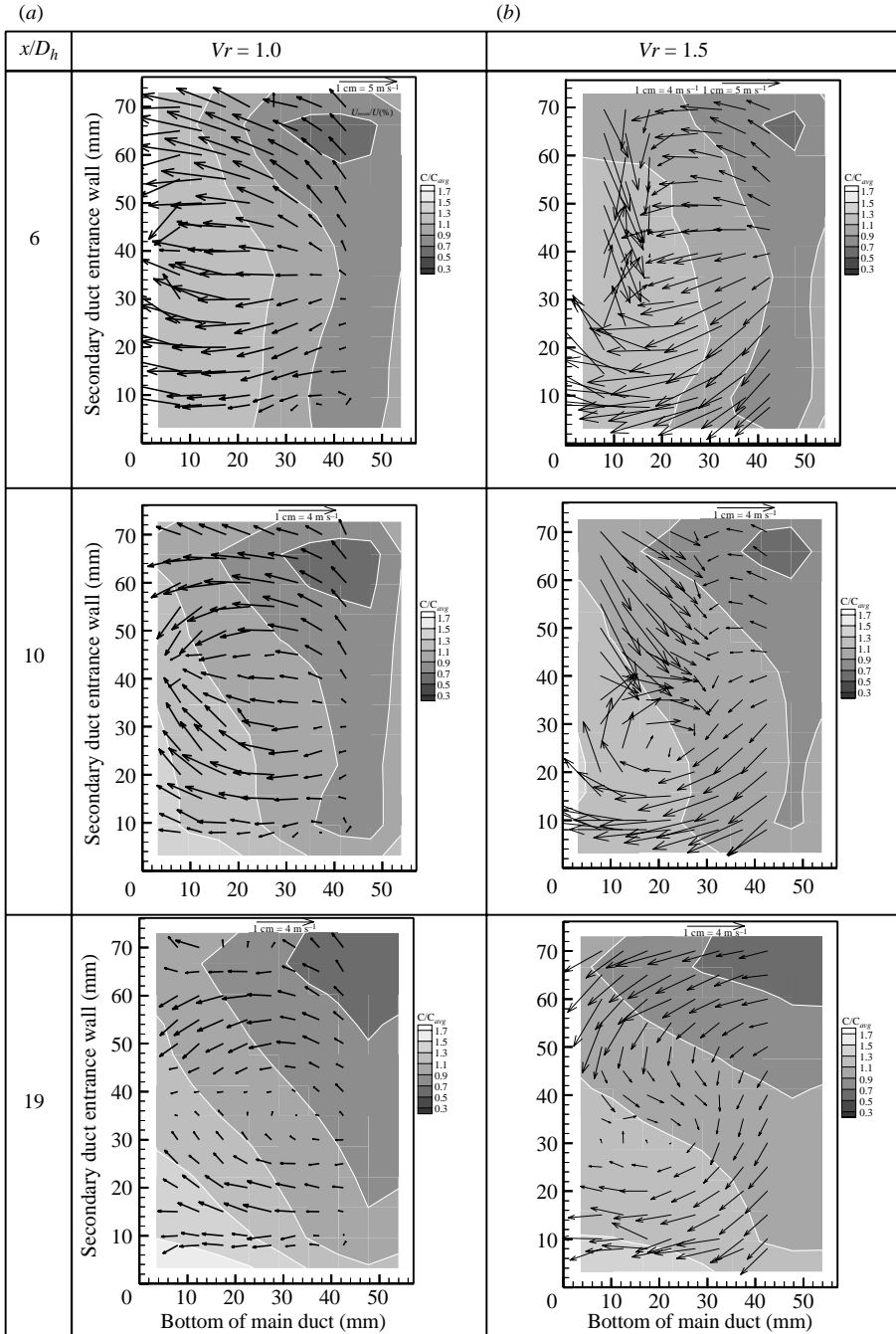


FIGURE 21. Mean scalar concentration-velocity field overlay and effect of development length, $\alpha = 48^\circ$, and (a) $Vr = 1.0$, (b) $Vr = 1.5$.

the top half of the duct. The secondary velocity vectors turn 90° towards the injection wall, whereas the vectors changed direction away from the injection wall between $x/D_h = 6$ and $x/D_h = 10$. Their relation to the concentration contours indicates that

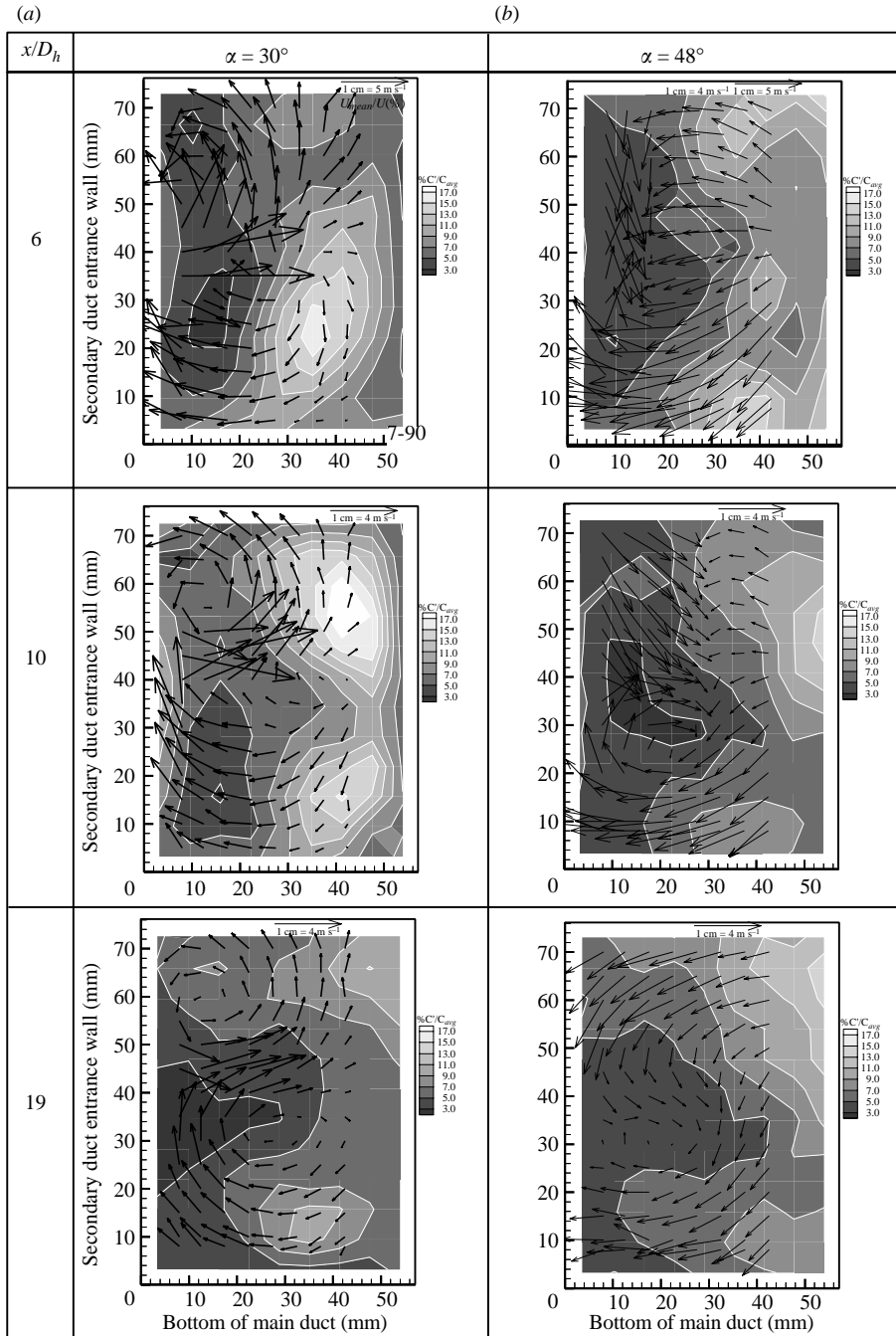


FIGURE 22. Concentration fluctuation/secondary-velocity field overlay and effect of development length, $Vr = 1.5$, and (a) $\alpha = 30^\circ$, (b) $\alpha = 48^\circ$.

the particle-lean region in the area will be decreasing in size at subsequent downstream locations.

Figure 22 presents CFM overlaid with secondary flow velocity vectors and serves to clarify one of the observations noted § 3. That is, regions of low fluctuation mark the

cores of the CRVP. The vortical structures are most evident in $Vr = 1.5$ cases, where they are expected to be strongest. Figures 22(a) and 22(b) show good correspondence with regions of low fluctuation (dark contours) to the apparent centres of the CRVP at $x/D_h = 6, 10$ and 19 . The action of the CRVP dominates the scalar mixing field. The lowest C' values occur at the spanwise centreline of the jet (figure 22 (lower)), where entrainment is highest.

4.3. JICF flow regimes

Over the parameter space investigated, three distinct flow regimes were identified. The first regime occurs for low velocity ratios and shallow injection angles, where the jet is immediately bent over by the crossflow and remains 'attached' to the wall. This is termed the 'wall jet regime'. It is prevalent for all velocity ratios and injection angles $< 30^\circ$. Flow visualization shows that a separation line is formed for all wall-jet cases. This regime is typified by a reattachment of the jet upstream of $x/D_h = 1$, a rapid decay in the strength of the CRVP, and lack of large-scale mixing across the duct for $x/D_h < 20$. Flows in this regime are ideally suited for film-cooling applications.

The second regime is the classical jet-in-crossflow condition, or 'lifted jet regime'. It is characterized by penetration of the wall boundary layer, the existence of a 'wake' region behind the jet, and the formation of the distinctive counter-rotating vortices. These structures dominate the scalar transport and result in high levels of (large-scale) scalar and velocity mixing both across the duct and between the CRVP as x/D_h is increased. This regime is prevalent starting with the $\alpha = 48^\circ$, $Vr = 1.5$ case and for all cases with α greater than 48° .

The transitional state between the 'wall jet' and 'lifted jet' regimes is the 'reattached jet regime', which occurs for injection angles between 30° and 48° , depending on velocity ratio. This regime is characterized by a well-defined CRVP and substantially better cross-duct mixing than in the wall-jet cases. The CRVP remains close to the wall and there is no definite 'wake' region evident in either the mixing or velocity data. As control parameters are increased, and the flow enters the reattached regime, the separation line described for the 'wall jet' regime grows into a separation bubble and eventually develops into a wake region as found in the 'lifted jet' regime.

A map is given in figure 23 to summarize these JICF regimes. These results are consistent with others reported in the literature. However, the values of velocity ratio that bound the regimes depend on the JICF configuration. For example, Sherif & Pletcher (1990) found that the borderline case between high and low velocity ratio jets occurs between $Vr = 1$ and 2 . Taylor & Watkins (1981) found that round jets remained attached to the wall for $\alpha \leq 30$ at $Vr = 6$ to 12 .

5. Summary and conclusions

A confined rectangular JICF was investigated experimentally. Three control parameters were varied in this study, velocity ratio ($Vr = 0.5, 1.0, 1.5$), injection angle ($\alpha = 18^\circ, 24^\circ, 30^\circ, 48^\circ, 60^\circ, 90^\circ$) and downstream distance ($x/D_h = 6, 10, 19$). The major results of the study are reiterated below and conclusions drawn.

5.1. Mixing parameters

The parameter space in this study was found to span three behavioural flow regimes. Within these regimes, the relative importance of the control parameters on the mixing process changes. This prevents a global characterization of the influence of these parameters. Therefore, each parameter will be evaluated individually and then the relative importance of each will be discussed in the context of the three flow regimes.

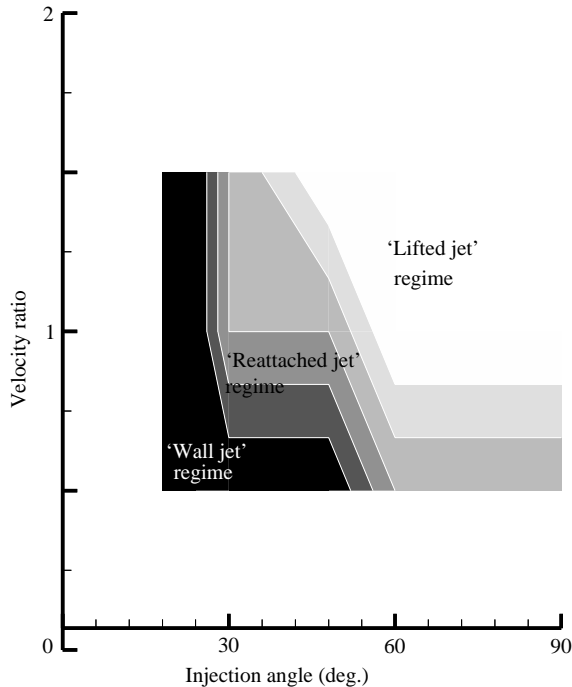


FIGURE 23. Flow regime map.

At any given injection angle, increasing velocity ratio increases jet penetration and CRVP strength and always improves mixing. For a given velocity ratio, increasing injection angle (for values greater than 30°) always results in better mixing. Increasing downstream distance, as expected, also always improves mixing, but not substantially in the wall-jet regime.

In the wall-jet regime, the dominant parameter is velocity ratio. Injection angle does very little to affect the flow for injection angles less than 30°. Mixing improves with downstream distance, but extremely slowly.

In the lifted jet regime, injection angle is the dominant parameter. Increasing the injection angle from 60° to 90° results in a significant and sudden change in the character of the mixing field. Mixing is dramatically improved as the flow develops from $x/D_h = 6$ to $x/D_h = 19$. Increasing velocity ratio from 0.5 to 1.5 provides only an incremental improvement in the flow mixing.

In the reattached regime, the three control parameters affect the mixing field nearly equally. This is evidenced by the fact that various combinations of parameters yield similar concentration field results, e.g. altering velocity ratio or injection angle, for a given streamwise distance, can achieve the same degree of mixing.

5.2. Asymmetry

It is reasonable to expect that a symmetrically shaped jet in uniform crossflow should produce symmetric flow structures. However, this is not the case in the current study nor in other related studies. Smith & Mungal (1998) reported asymmetric mean scalar fields for JICF originating from symmetric boundary conditions. Their work, and that of Kuzo (1995), shows that a JICF exhibits asymmetric flow fields even in the most symmetric geometric configurations. The CRVP fluctuates in size and strength at various streamwise locations. Both authors found that some conditions

and measurement locations were found to produce asymmetric scalar and velocity field results.

In the present study, most conditions and measurement locations produce asymmetric scalar and velocity field results, while only a small number produce symmetric results. It is perhaps not surprising that the more complex confined rectangular JICF produces an equally complex flow field to that of the canonical case.

5.3. Conclusions

In conclusion, a study of a confined, rectangular JICF was performed to simulate a simplified generic manufacturing process, which mixes two streams of products. The flow is more complex than a canonical unconfined round JICF, but has well-defined initial and boundary conditions to make it amenable to companion computational studies. It was found that the large-scale CRVP structures dominate the scalar mixing of the two streams. Three regimes of jet behaviour were identified. The flow physics and scalar mixing in each regime were discussed. Asymmetry of the velocity and scalar fields was identified for many combinations of parameters. The mechanism by which the asymmetry develops remains an open issue. Perhaps the asymmetry develops because of non-uniform amplification of the fundamental mechanism producing the CRVP. Further studies are required, both in the canonical JICF and in the more complicated case, to verify this hypothesis.

REFERENCES

- AJERSCH, P., ZHOU, J. M., KETLER, S., SALCUDEAN, M. & GARTSHORE, I. 1995 Multiple jets in a crossflow: detailed measurements and numerical simulations. *ASME-95-GT-9*.
- ANDREOPOULOS, J. 1982 Measurements in a jet-pipe flow issuing perpendicularly into a cross stream. *Trans. ASME I: J. Fluids Engng* **104**, 493–499.
- BEAN, H. S. (ed.) 1971 *Fluid Meters: Their Theory and Application*, 6th edn, pp. 47–79. American Society of Mechanical Engineers, New York.
- BECKER, H. A. 1977 Mixing, concentration fluctuations and marker nephelometry. In *Studies in Convection* (ed. B. E. Launder), vol. 2, pp. 45–139.
- BROADWELL, J. E. & BREIDENTHAL, R. E. 1984 Structure and mixing of a transverse jet in incompressible flow. *J. Fluid Mech.* **148**, 405–412.
- CHANG, H.-C. 1942 Aufrollung Eines Zylindrischen Strahles Durch Querwind. PhD dissertation, University of Göttingen. English translation: The roll-up of a cylindrical jet in cross flow, translated by K. S. Nagaraja and H. O. Schrade, USAF-ARL 73-0131, 1973.
- COELHO, S. L. V. & HUNT, J. C. R. 1989 The dynamics of the near field of strong jets in crossflows. *J. Fluid Mech.* **200**, 95–120.
- CRABB, D., DUARÃO, D. F. G. & WHITELAW, J. H. 1981 A round jet normal to a crossflow. *Trans. ASME I: J. Fluids Engng* **103**, 142–153.
- CROWE, C. T., GORE, R. A. & TROUTT, T. R. 1985 Particle dispersion by coherent structures in free shear flows. *Particulate Sci. Technol.* **3**, 149–158.
- CUSANO, D. M. 1999 Studies of a confined rectangular jet-in-crossflow. PhD thesis, School of Mechanical Engineering, Purdue University.
- DEMUREN, A. O. 1992 Multigrid acceleration and turbulence models for computations of 3-D turbulent jets in crossflow. *Intl J. Heat Mass Transfer* **35**, 2783–2794.
- DOERR, TH., BLOMEYER, M. & HENNECKE, D. K. 1995 Optimization of multiple jets mixing with a confined crossflow. *ASME-95-GT-313*.
- EATON, A. 1995 Influence of air–fuel jet momentum ratio and swirling on the performance of an axial swirl premixer. M S thesis, Purdue University.
- EATON, A. R., FREY, S. F., CUSANO, D. M., PLESNIAK, M. W. & SOJKA, P. E. 1996 Development of a full-field planar Mie scattering technique for evaluating swirling mixers. *Exps. Fluids* **21**, 325–330.

- EIFF, O. S., KAWALL, J. G. & KEFFER, J. F. 1995 Lock-in of vortices in the wake of an elevated round turbulent jet in a crossflow. *Exps. Fluids* **19**, 203–213.
- FINDLAY, M. J., HE, P., SALCUDEAN, M. & GARTSHORE, I. S. 1996 A row of streamwise-inclined jets in crossflow: measurements and calculations. *ASME-96-GT-167*.
- FRIC, T. F. & ROSHKO, A. 1994 Vortical structure in the wake of a transverse jet. *J. Fluid Mech.* **279**, 1–47.
- HALE, C. A., PLESNIAK, M. W. & RAMADHYANI, S. 2000 Structural features and surface heat transfer associated with a row of short-hole jets in crossflow. *Intl J. Heat Fluid Flow* **21**, 542–553.
- HAVEN, B. A. & KUROSAKA, M. 1996 The effect of hole geometry on lift-off behavior of coolant jets. *AIAA-96-0618*.
- HAVEN, B. A. & KUROSAKA, M. 1997 Kidney and anti-kidney vortices in crossflow jets. *J. Fluid Mech.* **352**, 27–64.
- HOLDEMAN, J. D. 1993 Mixing of multiple jets with a confined subsonic crossflow. *Energy Combust. Sci.* **19**, 31–70.
- HUMBER, A. J., GRANDMAISON, E. W. & POLLARD, A. 1993 Mixing between a sharp-edged rectangular jet and a transverse cross flow. *Intl J. Heat Mass Transfer* **36**, 4307–4316.
- JACQUIN, L. 1994 Phenomenological description and simplified modeling of the vortex wake issuing from a jet in a crossflow. *La Recherche Aéronautique* **2**, 117–133.
- JOHNSTON, J. P. 1999 Pitched and skewed vortex generator jets for control of turbulent boundary layer separation: a review. *ASME Paper, FEDSM-99-6917, FED-248*.
- JOHNSTON, J. P. & KAHN, Z. 1997 The origins of a dominant vortex from a pitched and skewed jet. *JSME Intl Conf. Fluids Engng July 1997, Tokyo*.
- JONES, W. P. & MCGUIRK, J. J. 1980 Computation of a round jet discharging into a confined cross-flow. *Turbulent Shear Flows II*, pp. 233–245. Springer.
- KAVSAOGLU, M. S., SCHETZ, J. A. & JAKUBOWSKI, A. K. 1989 Rectangular jets in a crossflow. *J. Aircraft* **26**, 793–804.
- KELSO, R. M., LIM, T. T. & PERRY, A. E. 1996 An experimental study of round jets in cross-flow. *J. Fluid Mech.* **306**, 111–144.
- KELSO, R. M., LIM, T. T. & PERRY, A. E. 1998 New observations of vortical motions of transverse jets. *Phys. Fluids* **10**, 2427–2429.
- KHAN, Z. U. & JOHNSTON, J. P. 2000 On vortex generating jets. *Intl J. Heat Fluid Flow* **21**, 506–511.
- KLINE, S. J. & MCCLINTOCK, F. A. 1953 Describing uncertainties in single sample experiments. *Mech. Engng*, **3**.
- KOUNALAKIS, M. E. 1990 Structure and radiation properties of turbulent diffusion flames. PhD thesis, University of Michigan.
- KRAUSCHE, D., FEARN, R. L. & WESTON, R. P. 1978 Round jet in a crossflow: influence of injection angle on vortex properties. *AIAA J.* **16**, 636–637.
- KUZO, D. M. 1995 An experimental study of the turbulent transverse jet. PhD thesis, California Institute of Technology.
- LEBCEUF, F., HUANG, G.-P., KULISA, P. & PERRIN, G. 1991 Model and computation of discrete jets in crossflow. *Eur. J. Mech.* **10**, 629–650.
- LEE, S. W., LEE, J. S. & RO, S. T. 1994 Experimental study on the flow characteristics of streamwise inclined jets in crossflow on flat plate. *J. Turbomachinery* **116**, 97–105.
- LEYLEK, J. H. & ZERKLE, R. D. 1994 Discrete-jet film cooling: a comparison of computational results with experiments. *J. Turbomachinery* **116**, 358–368.
- LIM, T. T., KELSO, R. M. & PERRY, A. E. 1992 A study of a round jet in cross-flow at different velocity ratios. *11th Australasian Fluid Mech. Conf. University of Tasmania, Hobart, Australia, December 14–18*.
- LISCINSKY, D. S. & TRUE, B. 1994 Planar Mie scattering measurements of scalar mixing. *SPIE* **2122**, 153–160.
- LISCINSKY, D. S., TRUE, B. & HOLDEMAN, J. D. 1996 Crossflow mixing of noncircular jets. *J. Propulsion Power* **12**, 225–230.
- LONG, M. B., CHU, B. T. & CHANG, R. K. 1981 Instantaneous two-dimensional gas concentration measurements by light scattering. *AIAA J.* **19**, 1151–1157.
- MCCANN, G. J. & BOWERSOX, R. D. W. 1996 Experimental investigation of supersonic gaseous injection into a supersonic freestream. *AIAA-96-0197*.

- MARGASON, R. J. 1993 Fifty years of jet in cross-flow research. Presented at Computational and Experimental Assessment of Jets in Cross-Flow. *AGARD-CP 534*, pp. 1–41.
- MARGASON, R. J. 1969 Analysis of the flow field of a jet in subsonic crosswind, in *Analytic Methods in Aircraft Aerodynamics*, NASA SP-228, pp. 683–702.
- MEHTA, R. D. & BRADSHAW, P. 1979 Design rules for small low speed wind tunnels. *Aeronaut. J. R. Aeronaut. Soc.* **83**–827, 443–449.
- MOFFAT, R. J. 1988 Describing the uncertainties in experimental results. *Exp. Thermal Fluid Sci.* **1**, 3–17.
- MORTON, B. R. & IBBETSON, A. 1996 Jets deflected in a crossflow. *Exp. Thermal Fluid Sci.* **12**, 112–133.
- NISHIYAMA, H., OTA, T., HAMADA, M. & TAKAHASHI, Y. 1993 Temperature fluctuations in a slightly heated slot jet issuing into a crossflow. *Exp. Thermal Fluid Sci.* **6**, 252–262.
- PATANKAR, S. V., BASU, D. K. & ALPAY, S. A. 1977 Prediction of the three-dimensional velocity field of a deflected turbulent jet. *Trans. ASME I: J. Fluids Engng*, December, 758–762.
- PETERSON, S. D. & PLESNIAK, M. W. 2002 Short-hole jet-in-crossflow velocity field and its relationship to film-cooling performance. *Exps. Fluids* **33**, 889–898.
- PETERSON, S. D. & PLESNIAK, M. W. 2004 Evolution of jets-in-crossflow emanating from short holes. *J. Fluid Mech.* **503**, 57–91.
- PRATTE, B. D. & BAINES, W. D. 1968 Profiles of the round turbulent jet in a cross flow. *J. Hydraul. Div. Proc. ASCE*, **94-HY6**, 53–64.
- RATHGEBER, D. E. & BECKER, H. A. 1983 Mixing between a round jet and a transverse turbulent pipe flow. *Can. J. Chem. Engng* **61**, 148–157.
- ROSENSWEIG, R. E., HOTTEL, H. C. & WILLIAMS, G. C. 1961 Smoke-scattered light measurements of turbulent concentration fluctuations. *Chem. Engng Sci.* **15**, 111–129.
- SAMIMY, M. & LELE, S. K. 1991 Motion of particles with inertia in a compressible free shear flow. *Phys. Fluids A* **3**, 1915–1923.
- SAVORY, E. & TOY, N. 1991 Real-time video analysis of twin jets in crossflow. *Trans. ASME I: J. Fluids Engng* **113**, 68–72.
- SAVORY, E., TOY, N. & AHMED, S. 1996 Experimental study of a plume in a crossflow. *J. Wind Engng Indust. Aerodyn.* **60**, 195–209.
- SGARZI, O. & LEBOEUF, F. 1997 Analysis of vortices in three-dimensional jets introduced in a cross-flow boundary-layer. *ASME-97-GT-517*.
- SHAUGHNESSY, E. J. & MORTON, J. B. 1977 Laser light-scattering measurement in a turbulent jet. *J. Fluid Mech.* **30**, 129–148.
- SHERIF, S. A. & PLETCHER, R. H. 1989 Measurements of the flow and turbulence characteristics of round jets in crossflow. *Trans. ASME I: J. Fluids Engng* **111**, 165–171.
- SHERIF, S. A. & PLETCHER, R. H. 1990 The physical and thermal characteristics of the subsonic jet in a cross stream – a review. *Mixed Convection Environ. Flows* **152**, 83–94.
- SHERIF, S. A. & PLETCHER, R. H. 1991 Jet-wake thermal characteristics of heated turbulent jets in crossflow. *J. Thermophys.* **5**, 181–191.
- SIMON, F. F. & CIANCONE, M. L. 1985 Flow visualization study of the effect of injection hole geometry on an inclined jet-in-crossflow. *Heat Transfer and Fluid Flow in Rotating Machinery: First Intl Symp. on Transport Phenomena. Honolulu, HI, USA*, pp. 170–192. Hemisphere.
- SIMONEAU, R. J. & SIMON, F. F. 1993 Progress towards understanding and predicting heat transfer coefficients in the turbine gas path. *Intl J. Heat Fluid Flow* **14**, 106.
- SMITH, S. H. 1996 The scalar concentration field of the axisymmetric jet-in-crossflow. PhD thesis, Stanford University.
- SMITH, S. H., LOZANO, A., MUNGAL, M. G. & HANSON, R. K. 1993 Scalar mixing in the subsonic jet-in-crossflow. *AGARD Jet in Cross Flow Symp.* pp. 141–147.
- SMITH, S. H. & MUNGAL, M. G. 1998 Mixing, structure and scaling of the jet-in-crossflow. *J. Fluid Mech.* **357**, 83–122.
- TAYLOR, P. & WATKINS, D. J. 1981 An investigation of inclined jets in a crosswind. *AGARD-CP-308, Paper 6*.
- TOY, N., SAVORY, E. & MCCUSKER, S. 1993 The penetration of twin turbulent jets in a crossflow. *Turbulent Mixing*, FED-174 ASME, pp. 71–76.
- WESTON, R. P. & THAMES, F. C. 1979 Properties of aspect-ratio-4.0 rectangular jets in a subsonic crossflow. *J. Aircraft* **16**, 701–707.

- YI, J. & PLESNIAK, M. W. 2002 Mixing of a particle-laden jet in a confined rectangular crossflow. *Powder Technol.* **125**, 168–178.
- YUAN, L. L. 1997 Large eddy simulations of a jet-in-crossflow. PhD thesis, Stanford University.
- YUAN, L. L. & STREET, R. L. 1998 Trajectory and entrainment of a round jet-in-crossflow. *Phys. Fluids* **10**, 2323–2335.
- YUAN, L. L., STREET, R. L. & FERZIGER, J. B. 1999 Large-eddy simulations of a round jet-in-crossflow. *J. Fluid Mech.* **379**, 71–104.